https://doi.org/10.5194/egusphere-2026-4254
Preprint. Discussion started: 3 September 2026

Observed large-scale trapping of gravity waves within the free troposphere

Giovanni Biagioli [1,★], Alexis Aubel [1,2,★], Riwal Plougonven [2], and Sandrine Bony [1]

[1]Laboratoire de Météorologie Dynamique/Institut Pierre-Simon Laplace (LMD/IPSL), Sorbonne Université, CNRS, Paris, France

[2]Laboratoire de Météorologie Dynamique/Institut Pierre-Simon Laplace (LMD/IPSL), École polytechnique, CNRS, Paris, France

★These authors contributed equally to this work.

Correspondence: Giovanni Biagioli (giovanni.biagioli@lmd.ipsl.fr)

Abstract. Gravity waves are a key dynamical feature of atmospheric flows, yet remain difficult to simulate and observe. However, on 15 August 2024, widespread wave signatures were observed over a broad region of the northeastern tropical Atlantic, with remarkable spatio-temporal coherence. One such packet was sampled in situ by the research aircraft operated within the MAESTRO field campaign, providing an ideal case study.

We perform a comprehensive characterization of the wave packet through a combination of in situ, remote sensing and radiosonde observations, using linear wave theory. Some incongruous features, notably the lack of coherence between horizontal and vertical wind perturbations, are additionally explained by an idealized cavity model. We also investigate the synoptic-scale environmental conditions: a well-mixed Saharan Air Layer in the lower-troposphere and significant upper-level shear delimited a clear free-tropospheric waveguide, allowing for long-lasting and long-range horizontal wave propagation, and a selection of specific wavelengths.

Building on this case study, we introduce a Trapping Likelihood Index, referred to as TraLI, which captures the environmental conditions conducive to gravity wave trapping at synoptic scales. This index can be computed over any chosen spatio-temporal domain using reanalysis data. For illustration, we analyze its variability over the region of interest during the year 2024, and show that its main variations are consistent with local climatology and previous studies of gravity wave trapping.

1 Introduction

Linear wave theory predicts internal gravity waves as a systematic response to vertical perturbations in a stratified atmospheric layer. Their genesis has long been studied in the context of flow-orography interactions (e.g. Queney, 1948; Nappo, 2012, and references therein), and their contribution to the circulation of the middle atmosphere (Fritts and Alexander, 2003) has motivated continuous efforts to improve their physical understanding and representation in atmospheric models (Alexander et al., 2010; Achatz et al., 2024). This perspective, combined with the development of parameterizations, has emphasized a vertical view of atmospheric Gravity Waves (GWs), with tropospheric sources, upward propagation, dissipation and ensuing forcing high aloft. Representing the nonlocal role of gravity waves in models encourages a focus on momentum fluxes (e.g. Ern

https://doi.org/10.5194/egusphere-2026-4254
Preprint. Discussion started: 3 September 2026

et al., 2004), identification and quantification of tropospheric sources (e.g. Hoffmann et al., 2013), and assessing the limitations of this framework (e.g. Bölöni et al., 2021).

Nonetheless, internal gravity waves also have local implications. Although linear wave perturbations average out over sufficiently large spatial and temporal scales, non-linearities of the atmospheric system can produce direct effects on the mean state. These include impacts on microphysical processes from wave-induced temperature fluctuations (e.g. Dörnbrack et al., 2002; Jensen et al., 2016), on the onset of boundary layer thermals (e.g. Lane. and Clark, 2002), and on tracer transport (e.g. Knop et al., 2026). Wave-induced shear fluctuations can also add to background shear, leading to instability and turbulence (e.g. Atlas et al., 2025; Kim et al., 2015). Some studies even suggest a direct coupling between the organization of convection and the wave field (Balaji and Clark, 1988; Lane and Zhang, 2011). Reverting to the global scale, the local mixing due to gravity waves also has a systematic impact on vertical transport in the tropical tropopause layer (Konopka et al., 2007; Glanville and Birner, 2017).

Internal gravity waves can also propagate over long horizontal distances when specific environmental conditions lead to wave trapping within an atmospheric layer. Trapping (or ducting) can be induced by vertical shear and/or stability variations, and, for the simplifying case of horizontally homogeneous flow, conditions conducive to trapping can be summarized through the Scorer parameter (Nappo, 2012). Again, this framework was first developed to understand waves in the lee of orography (Scorer, 1949; Wurtele et al., 1996), typically in a stable boundary layer that is capped by weaker stability and/or adverse winds (e.g. Fritts et al., 2003; Jia et al., 2019). The ground then serves as a reflecting boundary, allowing far downstream propagation in the absence of damping (Teixeira and Argaín, 2022). The region between the ground and the layer of weaker stability (where the waves cannot propagate and become evanescent) acts as a waveguide that allows for long-range horizontal propagation. Such a waveguide can also form in the interior of the atmosphere, between two evanescent layers (e.g. Isler et al., 1997). Until now, most attention has been devoted to the momentum fluxes and deceleration associated to mountain-induced waves, notably the trapped component (e.g. Durran, 1995; Georgelin and Lott, 2001; Teixeira and Argaín, 2022).

Trapped gravity waves have the potential to affect the troposphere over longer time and distances, can exhibit increased amplitudes (Nishi and Sugawara, 2026), which make them easier to detect and possibly lead to enhanced tropospheric impacts. This has motivated a renewed interest in trapped GWs, shifting attention to tropospheric waveguides further from the surface, and to waves not exclusively associated with orographic forcing (Trier and Sharman, 2018; Stephan, 2020; Vicari et al., 2024). These advances have been made possible by recent improvements in the resolution of numerical models and satellite products. In particular, the high spatial resolution of modern geostationary satellites, combined with the spatio-temporal coherence and persistence of trapped waves, enables their systematic detection. Vicari et al. (2024) takes advantage of this to investigate the occurrence of tropospheric waves with wavelengths of order 10 km over the eastern tropical Pacific, identifying small-scale wave signatures throughout four years of water vapour-sensitive satellite measurements from GOES-16. The occurrence of trapped waves appears more likely in the presence of significant shear in the upper troposphere, a configuration found during austral summer months (December, January, February). As an important limitation to their approach, the authors emphasize the significant uncertainty arising from identifying the trapped waves from remote sensing observations alone, and the lack

https://doi.org/10.5194/egusphere-2026-4254
Preprint. Discussion started: 3 September 2026

of complementary in situ observations to constrain key wave parameters. Addressing these gaps requires combining detailed observations of individual events with an assessment of the broader environmental conditions in which trapping occurs.

During the MAESTRO field campaign, conducted over the Cape Verde region in August-September 2024, a specific event attracted our attention: on 15 August, very clear oscillations in temperature and vertical velocity were detected in airborne in situ measurements, at a flight altitude of about 5.8 km. A half-dozen oscillations, very consistent between the two variables, dominate the measured timeseries, with a horizontal wavelength of about 6 km. Concomitantly, GOES-16 visible imagery reveals extensive wave signatures over a broad region of the northeastern tropical Atlantic, with remarkable spatio-temporal coherence, through most of the day. This well-documented event provides an opportunity to address several questions regarding the nature, origin and environmental control of the observed wave packet:

- Can the fluctuations observed in vertical velocity and temperature be interpreted as an internal gravity wave? If so, what are its characteristics? Do fluctuations of other variables concur?
- Which features of the environment are key to determining the wave signatures, including their remarkable spatio-temporal coherence? Can the large-scale conditions favour trapping?
- Is there evidence for a conspicuous source for the wave?
- Reverting to a frame larger than this specific case study, can we sketch which conditions are conducive to trapping, and make a preliminary assessment of their variability?

The paper is organized as follows. Section 2 introduces the MAESTRO field campaign and the observational datasets used in this study. Sections 3 and 4 present the results of the study. In particular, Section 3 provides a comprehensive characterization of the 15 August 2024 wave event and investigates the physical mechanisms responsible for its remarkable spatio-temporal coherence. Building on the physical understanding gained from this case study, Sect. 4 examines the climatology of conditions favourable to trapping in the Cape Verde region, extending the analysis beyond the specific case study. Finally, Sect. 5 summarizes our findings and discusses their broader implications for our understanding of GW trapping in the troposphere.

2 Data sources

2.1 The ORCESTRA and MAESTRO field campaigns

The Organized Convection and EarthCARE Studies over the Tropical Atlantic (ORCESTRA) campaign was an international research initiative primarily aimed at investigating the processes governing mesoscale convective organization in the tropics (Stevens et al., 2026). Conducted over the tropical Atlantic Ocean in August-September 2024, it comprised eight sub-campaigns addressing specific scientific objectives. The campaign integrated observations from a comprehensive suite of measurement platforms, including three research aircraft, a research vessel, the EarthCARE satellite, alongside complementary observations, such as radiosoundings (Winkler et al., 2026).

https://doi.org/10.5194/egusphere-2026-4254
Preprint. Discussion started: 3 September 2026

Within the framework of ORCESTRA, the French airborne sub-campaign MAESTRO (Mesoscale Organization of Tropical Convection) operated from Sal, Cape Verde (16.73° N, 22.94° W), with the SAFIRE ATR-42 research aircraft as its main observational platform. The ATR-42 is a twin-turboprop aircraft with an operational ceiling of 8 km and a typical cruise speed of 100 m s^{-1} (Bony et al., 2022). It performed flight patterns consisting of a sequence of straight and level legs of $\mathcal{O}(200\ \mathrm{km})$ horizontal extent at different altitudes, combined with spiral ascent and descent segments, sampling a variety of cloudy and clear-sky conditions.

The ATR-42 carried an extensive suite of in situ and multi-directional remote-sensing instruments. Remote-sensing instrumentation included, among other systems, the 95 GHz Doppler cloud radar RASTA (zenith- and nadir-pointing), and the high spectral resolution lidar LNG, operating at 355 nm and 532 nm in either zenith- or nadir-pointing mode. High-frequency in situ measurements of temperature, humidity, pressure, and the three wind components were acquired at 25 Hz (data acquisition described in Jaffeux et al., 2025), corresponding to a nominal along-track resolution of approximately 4 m at typical aircraft speed. Microphysical properties were sampled at 1 Hz using optical spectrometers and imaging probes, enabling retrieval of particle size distributions (PSDs) from 1.5 μm to 19 mm. Specifically, the payload consisted of the Fast Cloud Droplet Probe (FCDP), determining cloud droplet distributions and concentrations in the $1.5-50$ μm diameter range; the 2D Stereo probe (2D-S, $50-1270$ μm); and the High Volume Precipitation Spectrometer (HVPS, $0.15-19$ mm).

2.2 GOES-16 satellite data

In the present study, the airborne measurements are complemented by geostationary satellite observations. We analyze imagery from the Advanced Baseline Imager (ABI) aboard the GOES-16 geostationary satellite, positioned at 75.2° W and operating across 16 spectral bands from visible to infrared (Schmit et al., 2017). In particular, we use visible reflectance from ABI channel 2 (0.64 μm) and infrared (IR) brightness temperature from channel 13 (10.3 μm). These products have spatial resolutions of 0.5 km and 2 km at nadir, respectively ($\sim$ 1 km and $\sim$ 3 km over the Cape Verde region), and a temporal resolution of 10 minutes in full-disk mode.

3 Wave case study

This section focuses on the observations collected on 15 August 2024, during which the ATR-42 flew southeast of Sal (Figure 1a). Satellite imagery indicates that the synoptic-scale cloud field did not significantly differ from the typical conditions encountered throughout the campaign. Yet, s a more detailed examination of satellite and airborne observations reveal that this particular day was characterized by well-defined and ubiquitous wave-like signatures, which were considerably less prevalent on other days of the campaign.

3.1 Omnipresence of wave signatures in satellite imagery

Throughout the day on 15 August, GOES-16 visible imagery shows widespread wave-like signatures over a broad $\mathcal{O}(10^3\ \mathrm{km})$ region in the eastern tropical Atlantic around the Cape Verde islands. Cloud layers at different altitudes, as inferred from

https://doi.org/10.5194/egusphere-2026-4254
Preprint. Discussion started: 3 September 2026

IR brightness temperature imagery, exhibit ubiquitous modulations, with quasi-periodic structures indicative of wave activity at short spatial scales ($\leq$ 10 km; Figure 1b-f). These signatures are particularly well-defined across multiple wave cycles, displaying remarkable spatial and temporal coherence.

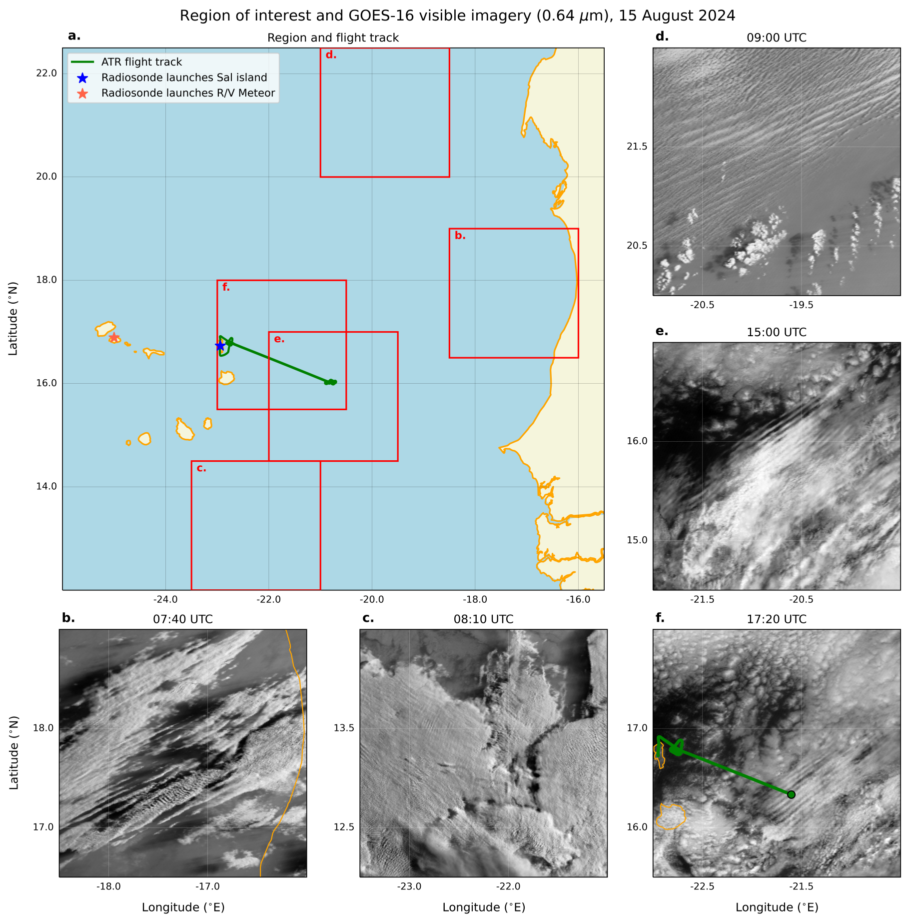

Figure 1. (a) Region of interest in the northeastern tropical Atlantic. The coastline is indicated by a solid orange line. The track of the ATR-42 research aircraft is shown in green, while the two radiosonde launch sites (Sal island and R/V Meteor moored at Mindelo) are represented as blue and red stars, respectively. Red boxes indicate the spatial domains corresponding to the subsequent panels. (b-f) GOES-16 visible imagery (0.64 μm) over various spatial domains of 2.5° $\times$ 2.5° at different times on 15 August 2024.

A first set of coherent periodic signals is visible in Figure 1 through the modulation of mid-level altocumulus decks (altitude $\sim$ 7 km; panels b,e,f) and lower-level clouds (panel d). These signatures have phase lines oriented along the SW-NE direction and wavelengths of about $5 - 10$ km. They recur throughout the day and across the region, appearing at locations as far as 500 km apart. One such wave pattern was sampled in situ by the ATR-42 during a straight, level flight leg, with the aircraft trajectory nearly perpendicular to the phase lines (see Figure 1f for the flight track). A second set of seemingly coherent periodic modulations of mid-level cloud decks can be detected at much shorter wavelengths and in various orientations (Figure 1b,c).

https://doi.org/10.5194/egusphere-2026-4254
Preprint. Discussion started: 3 September 2026

This second set of disturbances is also observed at multiple times and locations throughout the day. However, it was not sampled by the aircraft and is therefore not considered further in our study.

In addition, we note that the distinct quasi-periodic signatures detected in visible imagery can only reveal wave-induced vertical motions in the presence of clouds, while the observed signal likely also extends into clear-sky regions. This appears consistent with the observational analysis of Poujol and Bony (2024), who showed that vertical motions in clear-sky are primarily associated with gravity waves at the mesoscale, and is further corroborated by visual inspection of GOES-16 water vapor imagery. Consequently, the wave-induced cloud modulation shown in visible imagery likely represents only a small subsample of the underlying wave field, which on this day must have been even more widespread than depicted in Figure 1.

3.2 Airborne sampling of a wave packet

Between 17:15 and 17:25 UTC on 15 August 2024, the ATR-42 sampled a wave packet in situ during a straight, level flight leg at an altitude of 5.8 km (about 1 km below the top of the banded altocumulus cloud layer visible in Figure 1f). At that time, the aircraft was flying on a true heading of 109° and a true course of 112.5°, almost perpendicular to the phase lines.

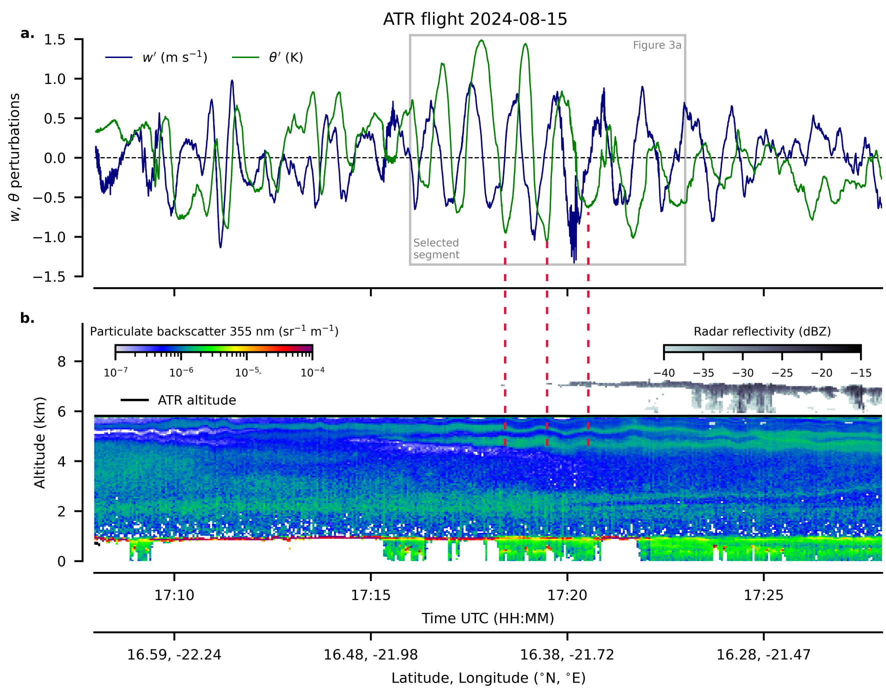

Figure 2. Along-track observations from the ATR-42 aircraft on 15 August 2024. (a) In situ measurements of vertical velocity (w', blue) and potential temperature (θ', green) perturbations. The dashed black horizontal line indicates zero perturbation and the grey box highlights the specific flight segment analyzed in the remainder of this study. (b) Remote-sensing observations: radar reflectivity from RASTA and 355-nm particulate backscatter from the nadir-pointing LNG lidar. The solid black horizontal line indicates the flight altitude. The dashed red vertical lines highlight the vertical coherence of the wave phase over a depth of approximately 2 km (see text for details).

https://doi.org/10.5194/egusphere-2026-4254
Preprint. Discussion started: 3 September 2026

Figure 2 presents observations collected along the flight track. in situ measurements of vertical velocity and potential temperature are shown in panel (a) as perturbations relative to the along-track background, denoted w' and θ' respectively. Panel (b) shows the radar reflectivity from RASTA and the 355-nm particulate backscatter from the LNG lidar in nadir-pointing mode. The remote-sensing observations indicate that the flight leg took place mostly in clear-sky conditions, until precipitation from the altocumulus layer was encountered at 17:23 UTC. Our analysis is limited to the clear-sky segment over which a well-defined quasi-periodic perturbation is apparent in all four variables. Their comparison provides evidence of vertical coherence over a depth of at least 2 km, as indicated by the red dashed lines in Figure 2.

This vertical coherence can be inferred directly from the relationship between displacement ζ and potential temperature anomaly θ' in a stably stratified atmosphere:

$$\theta' = -\zeta \frac{N^2 \overline{\theta}}{g}, \quad (1)$$

where N is the Brunt-Väisälä (or buoyancy) frequency, $\overline{\theta}$ is the background potential temperature, and g is gravity. The combined observations indicate that maxima in vertical displacement at flight level – identified by minima in θ' – align vertically with corresponding maxima in ζ about 1 km below, as inferred from the lidar backscatter field, and about 1 km above, where they manifest as either localized radar echoes (a few pixels) or a local thickening of the cloud layer in the RASTA signal.

In the following, we focus on the segment between 17:16 and 17:23 UTC, where the wave signal is most distinct. Figure 3 presents the corresponding time series of w', θ', zonal and meridional wind perturbations (u', v'), relative humidity with respect to liquid water and ice (RH_w, RH_i), and the evolution of the particle size distribution measured by the cloud probe array.

In particular, w' and θ' reveal a nearly monochromatic wave signal that remains coherent over multiple cycles (Figure 3a). In contrast, the horizontal wind perturbations do not display an equally clear signature, with the variability in u' and v' not consistently matching the wavelength observed in w' and θ' (panel b). Possible reasons for this discrepancy will be discussed in Section 3.5. The time series of relative humidity also include higher-frequency variability compared to θ', yet display a clear anticorrelation with it, at a similar dominant wavelength (Figure 3c). This behavior is expected, as upward displacement of air parcels in a stably stratified atmosphere produces a negative potential temperature perturbation relative to the environment and a corresponding increase in relative humidity. This increase, when superimposed on a high background RH, can lead to saturated conditions and the formation of condensate, which possibly manifests as the localized radar echoes observed in Figure 2b.

Finally, the PSD derived from the FCDP probe also shows a clear modulation at comparable wavelengths (panel d). Enhanced particle number concentrations occur in phase with the minima of θ' and the maxima of relative humidity. Based on the arguments presented in the Supplementary Material, we argue that the observed signal reflects the wave-driven vertical transport of large mineral dust particles from the underlying Saharan Air Layer (SAL; see Section 3.4), thereby hinting at a wave-induced modulation of the mid-tropospheric coarse aerosol population.

https://doi.org/10.5194/egusphere-2026-4254
Preprint. Discussion started: 3 September 2026

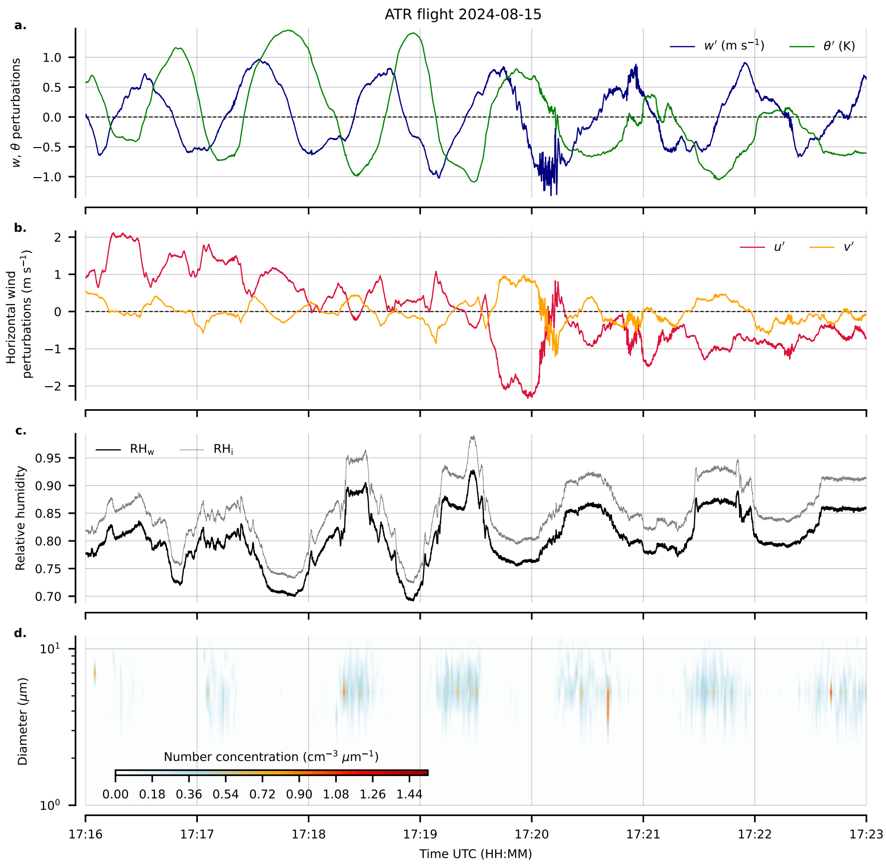

Figure 3. In situ airborne observations of the wave packet sampled between 17:16 and 17:23 UTC on 15 August 2024. (a,b) Vertical velocity (w', blue), potential temperature (θ', green), zonal (u', red) and meridional (v', orange) wind perturbations. (c) Relative humidity with respect to liquid water (RH_w, black) and ice (RH_i, grey). (d) Time-diameter representation of the particle size distribution from the onboard microphysics probes. The color scale indicates the number concentration.

3.3 Characterization of the wave packet

To interpret the dynamics and impacts of the event, a key question to address is what type of disturbance is responsible for the observed periodic signals. The horizontal wavelengths considered here ($\leq$ 10 km) are much shorter than those associated with planetary-scale modes of convectively coupled equatorial waves (Matsuno, 1966; Wheeler and Kiladis, 1999), which can be ruled out. Therefore, the primary mechanisms behind such quasi-periodic, small-scale signatures are either internal gravity waves, as predicted by linear wave theory (Nappo, 2012), or local non-linear perturbations, such as the Kelvin-Helmholtz instability (KHI). The latter can give rise to coherent structures (e.g. Luce et al., 2018), sometimes manifesting as regularly spaced billow clouds (Ludlam, 1967).

https://doi.org/10.5194/egusphere-2026-4254
Preprint. Discussion started: 3 September 2026

To discriminate between these phenomena, we compare the nearly sinusoidal signature sampled on 15 August with the sawtooth signal encountered for KHI (Luce et al., 2018). For illustration, a case observed with the same instruments on 25 August 2024 is presented in Appendix A. In situ measurements from this second flight (Figure A1a,b) show that the along-track wind perturbations (u', v', w') differ markedly from those observed in our case study. In particular, w' displays strongly asymmetric oscillations characteristic of non-linear shear-driven dynamics (e.g. Thorpe, 1969, 1971), that contrast with the nearly sinusoidal signature sampled on 15 August (Figure 3a). Estimates of the gradient Richardson number (Ri) from vertical atmospheric profiles provide additional evidence that the disturbances observed on 25 August were indeed associated with KHI. Conditions conducive to shear-driven instability are indicated by

$$\mathrm{Ri} = \frac{g}{\theta_v} \frac{\partial_z \theta_v}{(\partial_z u)^2 + (\partial_z v)^2} < 0.25 \tag{2}$$

where θ_v is the virtual potential temperature, (u, v) are the zonal and meridional wind components, and ∂_z denotes the partial derivative with respect to the vertical coordinate z (Stull, 1988). Examination of the vertical profiles from the radiosonde launched at 22:30 UTC, approximately 30 km from the aircraft sampling location, reveals a layer with $\mathrm{Ri} < 0.25$ exactly at the flight altitude (Figure A1c). In contrast, on 15 August, estimates of Ri at flight level are well above the critical threshold in both airborne measurements and radiosonde observations (Figure S2). Taken together, this body of evidence leads us to interpret the signal sampled on 15 August as gravity waves, for which linear wave theory can be used.

Within this framework, GWs are treated as small-amplitude perturbations to a stably stratified background state that varies only with height (Fritts and Alexander, 2003). The unforced momentum, mass, and energy conservation equations are linearized about a horizontally uniform, hydrostatic basic state and monochromatic wave solutions are then sought in the form

$$\xi'(x,y,z,t) = \tilde{\xi} \exp\left(i(kx + ly + mz - \omega t) + \frac{z}{2H_s} \right). \tag{3}$$

Here ξ' denotes a generic perturbation variable and $\tilde{\xi}$ its complex amplitude, i is the imaginary unit, k, l, and m are the zonal, meridional, and vertical wavenumbers, ω is the ground-relative frequency, and H_s is the density scale height.

In the following, we consider high-frequency waves for which rotational effects are negligible and assume that the vertical wavelength λ_z is small compared to the density scale height, allowing all terms proportional to H_s^{-1} to be neglected. Substitution of the form (3) into the linearized equations yields the GW dispersion (4) and polarization relations (5)-(8). The former reads (Fritts and Alexander, 2003)

$$\hat{\omega}^2 = \frac{N^2(k^2 + l^2)}{k^2 + l^2 + m^2} = N^2 \cos^2 \alpha, \tag{4}$$

where $\hat{\omega} = \omega - k\overline{u} - l\overline{v}$ is the intrinsic frequency, i.e., the frequency measured by an observer moving with the background flow ($\overline{u}$, $\overline{v}$), and α is the angle between the wave vector $\mathbf{k} = (k, l, m)$ and the horizontal plane.

https://doi.org/10.5194/egusphere-2026-4254
Preprint. Discussion started: 3 September 2026

Table 1. Background state and wave perturbation parameters, reported with the respective uncertainty ranges, for the 15 August 2024 case study.

N (rad s^{-1})	$\overline{u}$ (m s^{-1})	$\overline{v}$ (m s^{-1})	$\overline{\theta}$ (K)	$\lvert\tilde{w}\rvert$ (m s^{-1})	$\lvert\tilde{\theta}\rvert$ (K)	$\lvert\tilde{\zeta}\rvert$ (m)
1.4×10^{-2} (Period: 450 s)	-11.1	-1.1	324.8	1.0	1.2	150
$\pm0.2\times10^{-2}$	±0.3	±0.1	±0.1	±0.1	±0.1	±60

The polarization relations link the perturbation amplitudes and phases of the different variables within the wave field. Among others (Andrews et al., 1987; Fritts and Alexander, 2003; Plougonven et al., 2008):

$$\frac{\tilde{\theta}}{\overline{\theta}} = -i\frac{N^2}{g\hat{\omega}}\tilde{w}, \quad (5)$$

$$\tilde{w} = -i\hat{\omega}\tilde{\zeta}, \quad (6)$$

$$\tilde{u} = \frac{k}{l}\tilde{v}, \quad (7)$$

$$\tilde{u} = -\frac{mk}{k^2+l^2}\tilde{w}. \quad (8)$$

Applying these relationships to the wave packet sampled by the ATR-42 on 15 August, we can use the airborne measurements compiled in Table 1 to compute the wave characteristics, summarized in Table 2. The value for the Brunt-Väisälä frequency is derived from the radiosonde observations (see Section 3.4 for details, and for the uncertainty on this parameter), while the background state ($\overline{u}$, $\overline{v}$, $\overline{\theta}$) is calculated as the along-track mean of each variable between 17:16 and 17:23 UTC. The wave amplitudes are estimated as half peak-to-peak values from in situ measurements (Figure 3a) and, for $\lvert\tilde{\zeta}\rvert$, from lidar observations taken just below the flight altitude (Figure 2b).

We first use equation (5) to estimate the intrinsic frequency, yielding $\hat{\omega} = 5.4\times10^{-3}$ rad s^{-1}, which corresponds to an intrinsic period of 1160 s ($\sim$ 19 min), with the related uncertainty reported in Table 2. Equation (6) can be used to provide an independent estimate of the intrinsic frequency based on lidar measurements, yielding $(6.7\pm2.7)\times10^{-3}$ rad s^{-1}, albeit with substantially larger uncertainty, due to the 60m vertical resolution of the lidar product.

Equation (7) constrains the direction of horizontal phase propagation through the phase relationship between u' and v' (Figure 3b). Their respective time series were linearly detrended and band-pass filtered using a fourth-order Butterworth filter applied in forward-backward mode to avoid phase distortion. The cutoff frequencies were selected based on inspection of the Fourier transforms of u' and v' (see Section 3.5), with a robust phase opposition observed between u' and v', regardless of the specific cutoff values. A similar phase opposition is also detected in contemporaneous radiosonde measurements (Figure 4a; radiosonde launched about 150 km from the aircraft sampling location). To isolate the wave disturbance from the background flow, the vertical profiles of u and v from the radiosounding were processed following a commonly used methodology (Guest et al., 2000; Plougonven et al., 2003). The soundings were decomposed into background and perturbation profiles, with the

https://doi.org/10.5194/egusphere-2026-4254
Preprint. Discussion started: 3 September 2026

former defined as fourth-order polynomials fitted to the zonal and meridional wind components in the $2-10$ km layer using the least-squares method. The perturbation velocities were then obtained by subtracting the background flow from the observed wind profiles. The $2-10$ km layer was chosen to exclude regions of strong vertical wind shear that could contribute to the disturbance velocities, thereby ensuring that the extracted perturbations primarily represent wave activity. A clear phase opposition between u' and v' is visible in the radiosonde perturbation profiles between about $5-10$ km.

From Equation (7), the phase opposition implies that $k/l<0$, consistent with NW-SE horizontal phase propagation. To further constrain the propagation direction, we constructed the hodograph of horizontal wind perturbations from the airborne measurements. This is shown in Figure 4b, using the detrended and band-pass filtered time series with cutoff frequencies $1/40-1/20$ Hz. The hodograph was computed over a 4-min subsegment of the 17:16-17:23 UTC transect and shows an ellipse with eccentricity close to unity, consistent with the assumption of a pure GW (e.g. Lu et al., 2005; Alexander et al., 2023). The ellipse major axis indicates the direction of horizontal phase propagation, with an ambiguity of 180°; in the present case it corresponds to approximately $\phi=125°$ or $\phi=305°$, where ϕ denotes the azimuth of the horizontal phase propagation, measured clockwise from geographic north. This is in very good agreement with the propagation direction inferred from Figure 1f, given that the wave vector is perpendicular to the SW-NE phase lines.

The 180° ambiguity can be resolved using the phase relationship between w' and θ'. As already visible in Figure 3a, w' and θ' are in quadrature, with θ' lagging w' by a quarter of a period. This implies that the wave phases propagate in the positive along-track direction, which, given the true course of the aircraft (112.5°), yields $\phi=125°$. The physical reasoning underlying our inference is illustrated schematically in Figure 4c. We interpret the aircraft transect as an instantaneous snapshot of the wave field, an assumption justified by the high aircraft speed compared to the phase speed of the wave. As an example, we consider a location where, at time t, $w'>0$ and $\theta'=0$ (point B in Figure 4c), which corresponds to air in thermal equilibrium with the environment, forced upwards by the wave. In a stably stratified atmosphere, the ascending parcels will become colder than the surrounding environment (Eq. 1); consequently, at a slightly later time $t+dt$, $\theta'<0$ at the same location. In the present case, this temporal transition (from $\theta'=0$ to $\theta'<0$ at point B) is possible only if the wave pattern propagates in the positive along-track direction.

Since the wave horizontal propagation direction, $\phi=125°$, is almost parallel to the aircraft track, we can reasonably consider the sampled along-track wavelength to be close to the true horizontal wavelength λ_h. Estimating it from the time series of w' and θ' yields $\lambda_h \approx 6.5$ km, in good agreement with the wavelength inferred from the visible imagery in Figure 1f. Finally, the dispersion relation (4) provides an estimate of the vertical wavelength, $\lambda_z \approx 2.7$ km. Overall, these wave characteristics are consistent across different instruments and independent estimation methods, with linear wave theory successfully explaining most features of the sampled wave packet.

3.4 Large-scale environmental conditions and wave trapping

One peculiar characteristic, however, cannot be explained simply by the propagation of a linear GW: the vertical phase coherence observed in Figure 2. According to the dispersion relation (4), one would expect tilted phase propagation at an angle $\alpha>0°$ with the horizontal plane whenever $\hat{\omega}<N$, as in the present case. Both the near-vertical phase lines and the horizontal

https://doi.org/10.5194/egusphere-2026-4254
Preprint. Discussion started: 3 September 2026

Table 2. Characteristics of the gravity waves sampled in situ. The horizontal wave propagation azimuth ϕ is inferred from the hodograph (Figure 4), while the horizontal wavelength λ_h is estimated from the along-track in situ measurements (Figure 3a). The vertical wavelength λ_z and intrinsic frequency $\hat{\omega}$ are derived from the dispersion and polarization relationships (4) and (5), respectively. The intrinsic and ground-relative phase speeds, $\hat{c}$ and c, are computed according to their respective definitions (see text for more details).

$\hat{\omega}$ (rad s^{-1})	ϕ (°)	λ_h (km)	λ_z (km)	$\hat{c}$ (m s^{-1})	c (m s^{-1})
5.4×10^{-3} (Period: 1160 s)	125	6.5	2.7	5.6	−2.9
$\pm 1.7 \times 10^{-3}$	±3	±0.5	±0.6	±1.8	±1.8

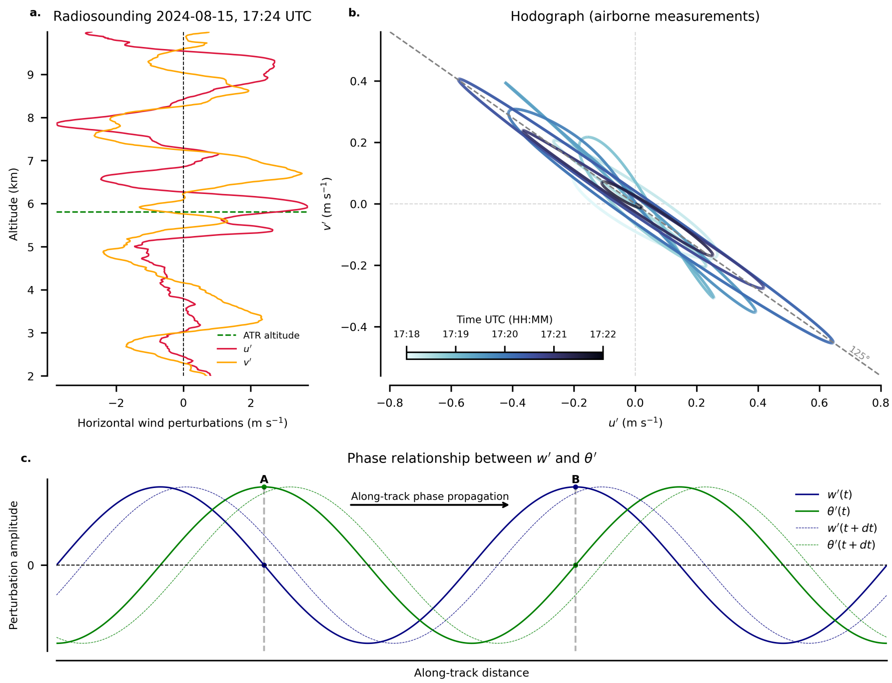

Figure 4. (a) Zonal (u', red line) and meridional (v', orange) wind perturbations relative to the background state, shown as a function of altitude in the $2-10$ km range and derived from the 17:24 UTC radiosounding on 15 August 2024 (see text for details). The dashed green horizontal line indicates the ATR-42 flight altitude at the wave sampling location. (b) Hodograph of horizontal wind perturbations relative to the along-track mean, derived from airborne measurements during the 17:18-17:22 UTC segment (see text for details) and colored for time evolution. The dashed grey diagonal line indicates the orientation of the major axis of the polarization ellipse. (c) Schematic of the phase relationship between vertical velocity (w', blue) and potential temperature (θ', green) perturbations, used to infer the direction of horizontal phase propagation. The fields at time t (solid lines) and $t+dt$ (dashed) are shown as a function of along-track distance. The dashed grey vertical lines indicate the state of air parcels at times t and $t+dt$, at two fixed locations A and B.

https://doi.org/10.5194/egusphere-2026-4254
Preprint. Discussion started: 3 September 2026

coherence over multiple wave cycles evident from satellite images (Figure 1f) point towards potential wave trapping (Lane. and Clark, 2002; Nappo, 2012; Stephan, 2020). The likelihood of such trapping strongly depends on the atmospheric background state (Stephan, 2020; Vicari et al., 2024).

We therefore examined the large-scale environmental conditions sampled on 15 August, using all radiosonde profiles collected within the ORCESTRA campaign on that day, along with observations from the spiral ascent and descent legs of the ATR-42 flight. The radiosonde data include launches from Sal (Cape Verde), as well as from the research vessel R/V Meteor, stationed at that time in Mindelo (Cape Verde; 16.89° N, 25° W), approximately 220 km West of Sal (Figure 1a). Most radiosonde launches provided both ascent and descent profiles (Winkler et al., 2026), which we included to increase the number of available samples and improve the spatial and temporal coverage of our analysis. Overall, these measurements cover a spatial extent of over 550 km in the zonal direction and 100 km in the meridional direction. Figure 5a,b aggregates all vertical profiles of potential temperature (θ) and water vapor mixing ratio (r_v). Lines are color-coded according to platform or launch location (blue: Sal; red: R/V Meteor; yellow: ATR-42), with lighter to darker shades representing the temporal evolution.

The observed thermodynamic structure is distinctive, ubiquitous across the sampled mesoscale region and persistent throughout the day. A well-mixed layer is present from the top of the boundary layer at approximately 1.5 km up to $5-5.5$ km. The nearly constant θ and r_v values, coupled with northeasterly winds and lidar observations of an aerosol layer reaching up to 5.5 km (see Figure 2b), are consistent with the presence of a Saharan Air Layer (SAL; Carlson and Prospero, 1972). Above this layer, dry static stability increases before decreasing again above roughly 10 km. As a complementary piece of evidence, we checked that this thermodynamic structure is robustly captured across comparable spatial scales by high-resolution numerical simulations performed as part of the ORCESTRA campaign (Stevens et al., 2026, see also Supplementary Material for details). The consistency between model output and our observations provides further confidence in the regional representativeness of the sampled environment. Finally, while this stratification was already evident in the 14 August radiosonde profiles (albeit less clearly defined), by 16 August the well-mixed layer had significantly eroded.

We next explore whether the distinctive background state of 15 August can support wave trapping. Within the framework of linear GW theory, the possibility of vertical trapping can be assessed using the Scorer parameter S (Scorer, 1949; Crook, 1988; Stephan, 2020), where

$$S^2 = \frac{N^2}{(U_h - c)^2} - \frac{1}{(U_h - c)} \frac{\partial^2 U_h}{\partial z^2}, \tag{9}$$

with U_h the projection of the horizontal wind in the direction of horizontal wave propagation and c the ground-relative horizontal phase speed. This parameter appears in the wave equation for linear GWs, the Taylor-Goldstein equation, which can be written as (Nappo, 2012)

$$\frac{\partial^2 \tilde{w}}{\partial z^2} + (S^2 - k_h^2)\tilde{w} = 0, \tag{10}$$

where k_h is the horizontal wavenumber of an internal wave. We note that the scale-height compressibility terms have been neglected following the assumptions stated in Section 3.3. The Taylor-Goldstein equation defines the condition for vertical

https://doi.org/10.5194/egusphere-2026-4254
Preprint. Discussion started: 3 September 2026

trapping: a layer with $S^2 > k_h^2$ (where Eq. 10 admits propagating solutions) has to be sandwiched either between two layers with $S^2 < k_h^2$ (where the wave becomes evanescent) or between the ground and one such layer.

In the following, we analyze the vertical profiles from the radiosonde launched from Sal (Cape Verde) at 17:24 UTC, the closest in space and time to the wave sampling by the aircraft. The vertical profile of N^2 (Figure 5c) shows the aforementioned well-mixed layer up to about 5 km, as well as an additional weakly stratified layer between $11-13$ km. The stratification is strongest between $5-8$ km, and the average N in this layer was used to estimate the wave parameters as described in Section 3.3. The uncertainty in N is of leading order for the computation of wave parameters (Table 2). To account for the sensitivity of these estimates, we defined a representative range for N. The lower bound is the average N over the entire $5-10$ km stably stratified layer, whereas the upper bound is the average N over a 1km layer centered on the absolute maximum stratification in the mid-troposphere. The corresponding range describes the uncertainty in N reported in Table 1.

To compute the Scorer parameter, the stability and wind profiles, as well as their derivatives, were smoothed using a local least-squares second-order polynomial filter, with a 2km smoothing window. The resulting profiles are shown as thick lines in Figure 5c,d. In addition, the values of c and k_h were derived in Sect. 3.3 (Table 2). The vertical profile of S^2 (Figure 5e) indicates favourable conditions for wave trapping, with a well-defined waveguide identified between 5 and 10 km.

The vertical structure of S^2 is primarily attributed to its first term (Eq. 9), which dominates over the other terms at most altitudes and combines the effects of background stratification and wind shear, implicitly captured by the vertical variability of U_h (Stephan, 2020). In the lower part of the waveguide, the peak in S^2 results from both the increase in N^2 above the SAL and a slight reduction in $|U_h - c|$; in the upper part, variations in S^2 are mostly controlled by the wind profile. Below the waveguide, the small values of S^2 are associated with weak stratification, while above it the increase in wind speed leads to a decrease in S^2, effectively defining the upper boundary of the duct. In conclusion, for the observed horizontal wavelength, the identified waveguide is a joint thermal-wind duct (Dong et al., 2021), with wave reflection induced by vertical changes in stability at the lower boundary and in the wind at the upper boundary.

3.5 Poly-chromatic model of wave-trapping

A further question remains as to why the dominant wavelengths differ markedly between (w', θ') and (u', v') as seen in Figure 3a,b. To better understand this feature of the observed wave signal, we consider an idealized configuration consisting of a two-dimensional waveguide of depth H, characterized by a constant stable stratification $N > 0$ and no background wind shear, sandwiched between two neutrally stratified layers ($N = 0$) of infinite depth. Assuming invariance in the transverse direction, we define a coordinate system (x, z), with x aligned with the direction of horizontal phase propagation. This configuration is analogous to the well-known problem of a laser cavity in optics (Gretarsson, 2021), and is analyzed using the same formalism. Hereafter, u' denotes the projection of the horizontal wind along the x-direction, and we consider the two-dimensional form of equations (3)-(10).

Solving Eq. (10) in this configuration for waves with a common intrinsic frequency $\hat{\omega}$, on a continuous spectrum of horizontal wavenumbers k, yields vertically propagating waves within the waveguide and evanescent solutions in the neutral regions. The

https://doi.org/10.5194/egusphere-2026-4254
Preprint. Discussion started: 3 September 2026

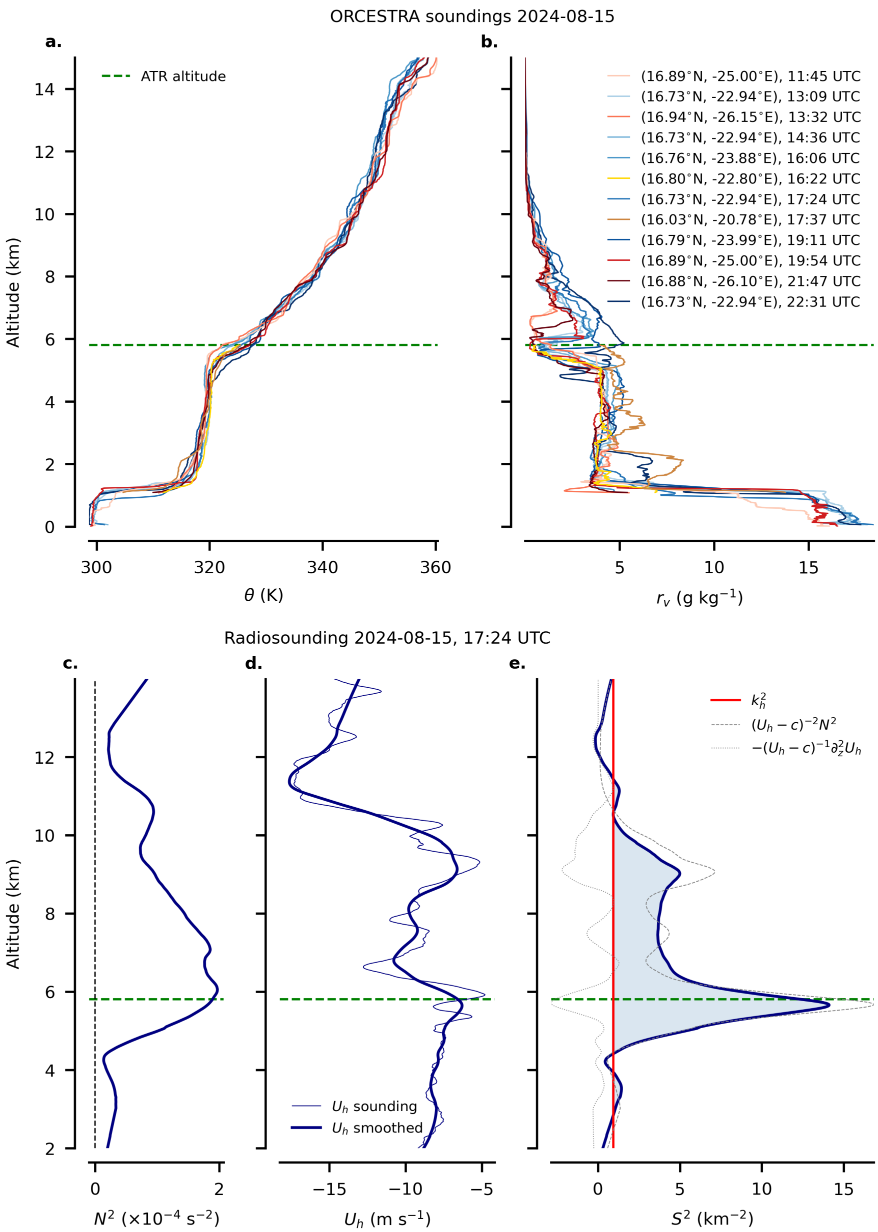

Figure 5. (a,b) Vertical profiles of potential temperature (θ) and water vapour mixing ratio (r_v) from ORCESTRA radiosoundings, together with profiles from ATR-42 spiral ascent and descent legs on 15 August 2024. Colors indicate platform or launch location (blue: Sal, red: R/V Meteor, yellow: ATR-42), with lighter to darker shades representing temporal evolution. The legend provides the start coordinates (latitude, longitude) and time of each sounding. (c-e) Vertical profiles from the 17:24 UTC radiosounding on the same day. (c,d) Smoothed vertical profiles of N^2 and U_h, the wind projected along the wave propagation direction (thin line for raw profile in panel d; see main text for smoothing details). (e) Vertical profile of the squared Scorer parameter (S^2, Eq. 9), together with its two terms (see legend). The red vertical line denotes the squared horizontal wavenumber (k_h^2) of the sampled wave packet, and blue shading highlights the region where vertical propagation is allowed ($S^2 > k_h^2$, Eq. 10). In all panels, the dashed green horizontal line marks the ATR-42 flight altitude at the wave sampling location.

https://doi.org/10.5194/egusphere-2026-4254
Preprint. Discussion started: 3 September 2026

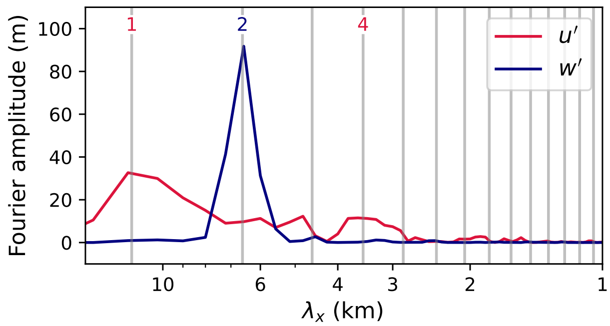

Figure 6. Fourier decomposition of the horizontal (red) and vertical (blue) wind components, obtained from in situ measurements. The transect was taken here from 17:14 to 17:25 UTC, covering the longest available interval with an observed gravity wave signal to improve the sampling of longer wavelengths. Vertical bars denote the theoretical modes of standing waves for a waveguide of depth $H = 3.2$ km (see text for details).

330 vertical wavenumber m and the e-folding length scale δ of evanescent modes in the neutral layers are given by

$$\begin{cases} m & = \pm k \frac{\sqrt{N^2 - \hat{\omega}^2}}{\hat{\omega}}, \\ \delta^{-1} & = \pm k. \end{cases} \tag{11}$$

At the interface between the stratified layer and a neutral region, continuity of u' and w' is imposed. Applying the polarization relation derived from mass continuity (Eq. 8) leads to a linear system relating the amplitudes of the incident, reflected, and evanescent waves. Denoting the reflection and transmission coefficients as $\mathscr{R}$ and $\mathscr{T}$, respectively, we obtain:

335
$$\begin{cases} \mathscr{R} = 1 - \frac{2\hat{\omega}^2}{N^2} + i\frac{2\hat{\omega}\sqrt{N^2 - \hat{\omega}^2}}{N^2} = |\mathscr{R}|e^{i\psi}, \\ \mathscr{T} = 2 - \frac{2\hat{\omega}^2}{N^2} + i\frac{2\hat{\omega}\sqrt{N^2 - \hat{\omega}^2}}{N^2}. \end{cases} \tag{12}$$

where $\psi = \arctan\left(\frac{2\hat{\omega}\sqrt{N^2 - \hat{\omega}^2}}{N^2 - 2\hat{\omega}^2}\right)$ indicates the phase shift upon reflection at the waveguide boundaries.

We note that the modulus of the reflection coefficient satisfies $|\mathscr{R}| = 1$ and that these coefficients depend only on the wave intrinsic frequency and environment stability, not on k. This indicates complete reflection at both interfaces in this idealized configuration for all values of k. Upward- and downward-propagating waves within the waveguide can interfere constructively and form standing wave patterns. Resonant modes are obtained when the total phase shift accumulated over a complete cycle within the waveguide satisfies

$$mH - \psi = n\pi, \qquad n \in \mathbb{N}^*. \tag{13}$$

This gives rise to a selection of vertical wavelengths, hence, through (11), to a selection of horizontal wavelengths for specific trapped modes of x-propagating z-standing waves.

We now apply this idealized model to our case study, using the values of N and $\hat{\omega}$ previously derived (Tables 1 and 2). The resulting selected horizontal wavelengths (13), computed for a waveguide of depth $H = 3.2$ km, are illustrated in Figure 6 as

https://doi.org/10.5194/egusphere-2026-4254
Preprint. Discussion started: 3 September 2026

thin vertical lines, annotated with their respective mode number n. The Fourier decomposition of the horizontal and vertical wind components measured along the flight track are overlaid. These theoretical modes align well with peaks in the Fourier decomposition of either u' or w', for many of the predicted wavelengths (w': modes 2, 3, 6; u': modes 1, 3, 4, 8).

Among the different trapped modes, we investigated the vertical structure of three selected modes which have the most distinct imprint in the Fourier decomposition: the modes 1, 2 and 4 (Figure 7). As expected from wave theory, the strongest signal is observed for the lower harmonics (modes 1 and 2, Figure 6). Interestingly, these trapped modes project predominantly onto either horizontal (modes 1 and 4) or vertical (mode 2) velocity components, not on both. Figure 7 provides an explanation for this: in trapped modes of GWs, the vertical structure of the wave displays a $\pi/2$ phase shift between the nodes/antinodes of u' and w'. Taking the lower boundary of the waveguide at $z = 4.5$ km, consistent with observations (Figure 5e), we note that, at flight altitude (dashed green line in Figure 7), the aircraft samples nodes of w' and antinodes of u' for modes 1 and 4, while, for mode 2, it samples nodes of u' and antinodes of w'. This theoretical prediction qualitatively accounts for the distribution of spectral peaks (Figure 6) and explains why u' and w' appear to be dominated by different wavelengths in the airborne data (Figure 3a,b).

The value $H = 3.2$ km was chosen so that the selected modes best align with the Fourier decomposition in Figure 6. We note that the waveguide depth is of the right order of magnitude relative to that inferred from the vertical profile of the Scorer parameter (Figure 5e), albeit shallower. This discrepancy likely stems from the assumption of a single constant N value over the full depth of the waveguide in the simple model, as discussed in the Supplementary Material.

Finally, using the measured wind series, we isolated the signal associated with individual modes via a Butterworth band-pass filter centered at their respective wavelengths. This confirms coherent wave activity at these scales. In addition, the resulting mode-specific hodographs (Figure S4) display the same orientation as that shown in Figure 4b, which implies that the higher-order harmonics share the same direction of propagation, hinting at a common source. This justifies the use of a common intrinsic frequency $\hat{\omega}$ in the simple model. In conclusion, the peaks of energy across the Fourier space not only co-exist through trapping and wavelength selection, but also originate from the same source and belong to the same trapped wave packet.

4 Climatology of trapping-favourable conditions

The analysis of the 15 August 2024 case study demonstrates that the vertical structure of the atmosphere was particularly favourable for the ducting of GW packets. Moreover, the horizontal homogeneity of the background environment, as inferred from radiosoundings and numerical model output, suggests that the waveguide is not merely a local feature, but rather a characteristic of the large-scale flow in which the waves are propagating. A question arises as to whether this was an isolated event or if this region in the eastern tropical Atlantic frequently exhibits environmental conditions conducive to large-scale wave trapping. We therefore expand our analysis to a regional climatological perspective, using ERA5 reanalysis data (Hersbach et al., 2020).

https://doi.org/10.5194/egusphere-2026-4254
Preprint. Discussion started: 3 September 2026

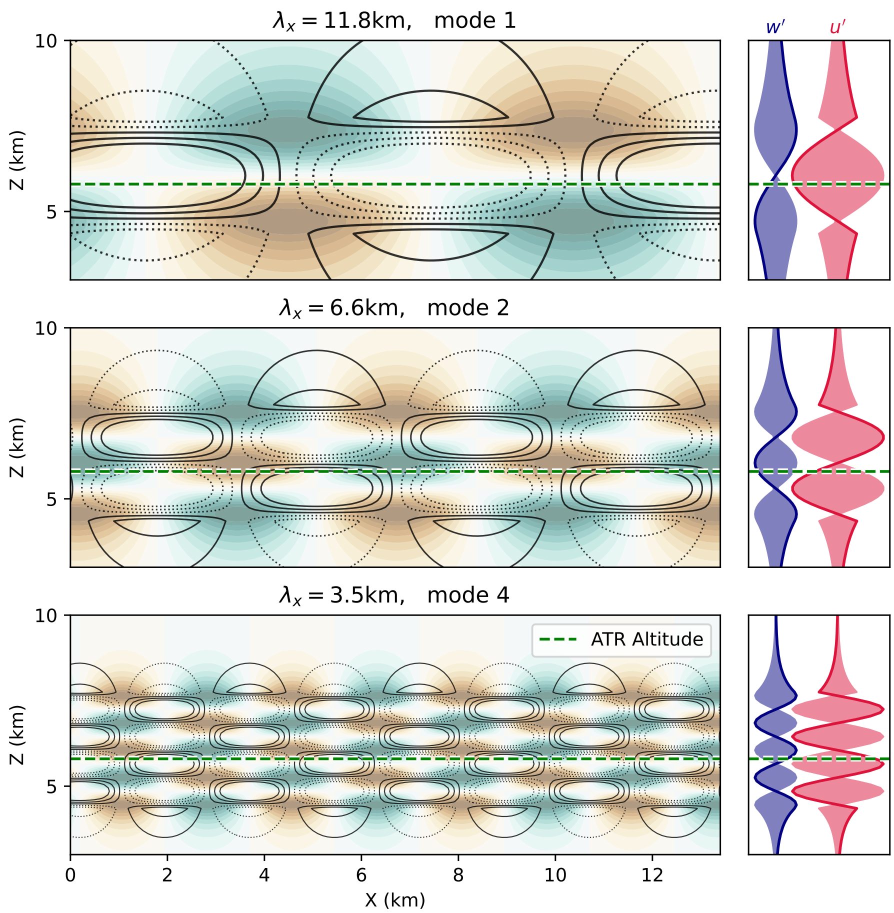

Figure 7. Selected modes of x-propagating z-standing gravity waves, trapped in an idealized stable layer (see text for details). The left column shows the instantaneous 2D wave structure, with w' as shading and u' as contours (dotted for negative values). The right column displays the nodes and antinodes of w' (blue) and u' (red) sampled along a constant-altitude flight leg. In all panels, the dashed green horizontal line indicates the flight altitude of the aircraft.

https://doi.org/10.5194/egusphere-2026-4254
Preprint. Discussion started: 3 September 2026

Within this framework, a direct computation of the Scorer parameter (9) is not feasible, given the lack of information regarding potential horizontal phase speeds c. To overcome this limitation and identify conditions conducive to wave reflection and possible ducting within the free troposphere, we seek a suitable proxy for S^2. For instance, Vicari et al. (2024) used the Richardson number (Eq. 2), since, like the Scorer parameter, it depends on both the vertical stratification and wind shear, identified as leading mechanisms of wave trapping. In this study, we propose a simplified formulation of the Scorer parameter, more closely aligned with the original definition than Ri. To this end, we make the following simplifications:

(1) We retain only the first term of S^2 (Eq. 9), $N^2(U_h - c)^{-2}$, which strongly dominates in our case (Figure 5e), as well as in other previous studies (Lane. and Clark, 2002; Stephan, 2020).

(2) We assume $|c| \ll |U_h|$, following previous studies (e.g. Kottayil et al., 2024). While this simplification is prompted by the general unavailability of the horizontal phase speed, it remains acceptable in our case (see Tables 1, 2 and Figure 5d) and for our purposes.

(3) We project the vertical wind profile $\mathbf{U}(z)$ along the mean direction ϕ_0 of upper-tropospheric flow, averaged over the height range corresponding to the $100-200$ hPa pressure layer. This assumes a critical role of the wind only in upper-level wave reflection, as further discussed below.

We can thus define a simplified version of the Scorer parameter:

$$S_0^2(z) = \frac{N^2}{(\mathbf{U}\cdot\mathbf{e}_{\phi_0})^2} \qquad (14)$$

where $\mathbf{e}_{\phi_0}$ is the unit vector along ϕ_0. Projecting the wind along its upper-tropospheric direction assumes that the variations of the background wind that matter most are those associated to the upper-troposphere, where the strongest winds are commonly found. This ensures that S_0^2 is minimized (i.e., the potential for wave reflection is maximized) in the upper troposphere. If conditions favourable for trapping are present, this will first be possible for waves propagating along the direction ϕ_0. We note that both assumptions (2) and (3) establish a conservative criterion: a vertical profile that does not allow for wave trapping for optimal directional conditions will not support wave trapping at all. Conversely, assuming a field of randomly distributed GW sources, waves propagating along ϕ_0 with anti-parallel U_h and c are those most likely to be selected and ducted.

This directional projection represents a conceptual simplification specifically designed to capture the wind-induced upper-level wave reflection identified in our case study (Figure 5c,d,e). This approach is consistent with previous findings on wave trapping in sheared flows (Stephan, 2020; Vicari et al., 2024) and is further justified by the analysis of the radiosoundings conducted throughout the MAESTRO campaign. Indeed, a systematic comparison of the vertical profiles of u, v and N^2 reveals that the wind field variability is predominantly concentrated in the upper-troposphere (Figure S5b) and strongly dominates over the essentially invariant upper-tropospheric stratification (Figure S5a). This leads us to hypothesize that any upper-level wave reflection would be mostly caused by the wind, thereby justifying the projection along the direction of ϕ_0. Computing S_0 on radiosounding profiles effectively isolates the wind features expected to control the upper boundary of the waveguide (Figure S5c). Unlike the Richardson number, whose vertical profiles are dominated by high-frequency noise (Figure S5d), S_0 provides a much cleaner signal with high temporal and vertical coherence.

https://doi.org/10.5194/egusphere-2026-4254
Preprint. Discussion started: 3 September 2026

In the following, we specifically target small-scale waves ($\lambda_h \sim 10$ km) trapped within an elevated layer in the free troposphere, as in our case study. To identify a potential waveguide, we search for lower- and upper-tropospheric layers where $S_0(z)$ drops below the threshold value $S_c = 6 \cdot 10^{-4}$ m^{-1}, corresponding to $\lambda_h = 10$ km. These potential reflection levels are sought within two distinct altitude ranges, operationally defined, with a slight abuse of notation, in terms of pressure levels as Z_{LT} between 900 and 600 hPa, and Z_{UT} between 400 and 100 hPa, respectively.

For a fixed horizontal domain $\mathscr{D}$, treated as an ensemble of vertical profiles $S_0(z)$ at a given time t, all projected along the direction of domain-mean upper tropospheric wind, we identify the profiles that satisfy the condition $S_0(z) \leq S_c$ in both Z_{LT} and Z_{UT} simultaneously. We then define the Trapping Likelihood Index (TraLI) as the fraction of such profiles within $\mathscr{D}$:

$$\mathrm{TraLI} = \frac{\mathrm{card}\,\mathscr{A}}{\mathrm{card}\,\mathscr{D}}, \text{ with } \mathscr{A} = \left\{ S_0(z) \in \mathscr{D} \;\middle|\; \begin{array}{c} \exists\, z_1 \in Z_{\mathrm{LT}},\; z_2 \in Z_{\mathrm{UT}} \\ S_0(z_1) < S_c \text{ and } S_0(z_2) < S_c \end{array} \right\}. \tag{15}$$

This quantifies the fractional coverage of conditions conducive to wave trapping within $\mathscr{D}$, which we interpret as the likelihood that the large-scale environment acts as a waveguide. Similarly, we can define a lower-TraLI and an upper-TraLI as the fraction of profiles within $\mathscr{D}$ meeting the reflection criterion $S_0 \leq S_c$ in Z_{LT} and Z_{UT} individually. Therefore, while these individual indices quantify the regional extent of lower- and upper-level reflectors, TraLI strictly requires their simultaneous occurrence to establish a free-tropospheric waveguide.

In the following analysis, we consider a domain of $10° \times 10°$ centered around Sal (Cape Verde), and compute the vertical profiles of S_0 using ERA5 reanalysis data (0.25° horizontal resolution, 37 vertical pressure levels, hourly temporal resolution). For the scope of this study, only the timesteps at 12:00 UTC are considered to provide a single daily value of TraLI, as its predominant variability occurs at longer timescales. Figure 8 presents the evolution of the lower- and upper-TraLI throughout 2024 (panel a; as a horizontal calendar, with one week per column and months advancing from left to right), together with representative GOES-16 visible images for selected days characterized by high TraLI values; the locations where conditions favourable to wave trapping are met (set $\mathscr{A}$ in eq. 15) are overlaid in red (panels b, c, d). The occurrence of trapped waves was inferred from the presence of banded cloud patterns in visible imagery and further confirmed by the inspection of GOES-16 water vapour images for clear-sky wave-induced modulation.

During the MAESTRO campaign period (August-September 2024), both lower- and upper-TraLI reach near-maximum values on 15 August (outlined in red in Figure 8a), exceeding 60%. A few other days – most notably 2, 10, 14 August – also exhibit high values of lower- and upper-TraLI and consistently show conspicuous and persistent wave activity over large spatial scales in GOES-16 visible imagery. Extending this analysis beyond the campaign period, this remains true for the other days with the largest TraLI values (outlined in yellow). A strong TraLI appears to be sufficient for free-tropospheric GW trapping; however, some days with weak TraLI (either upper-, lower- or both) also present wave activity, indicating that a strong TraLI is not a necessary condition.

The profile-wise definition of S_0 also allows us to investigate its regional variability, with a widespread presence of lower- and upper-tropospheric reflecting layers leading to large TraLI values. In panel b, wave activity is visible at 23° W, 13 – 17° N, well within $\mathscr{A}$. The orientation of the crests suggests a wave vector nearly aligned with the upper-tropospheric wind direction

https://doi.org/10.5194/egusphere-2026-4254
Preprint. Discussion started: 3 September 2026

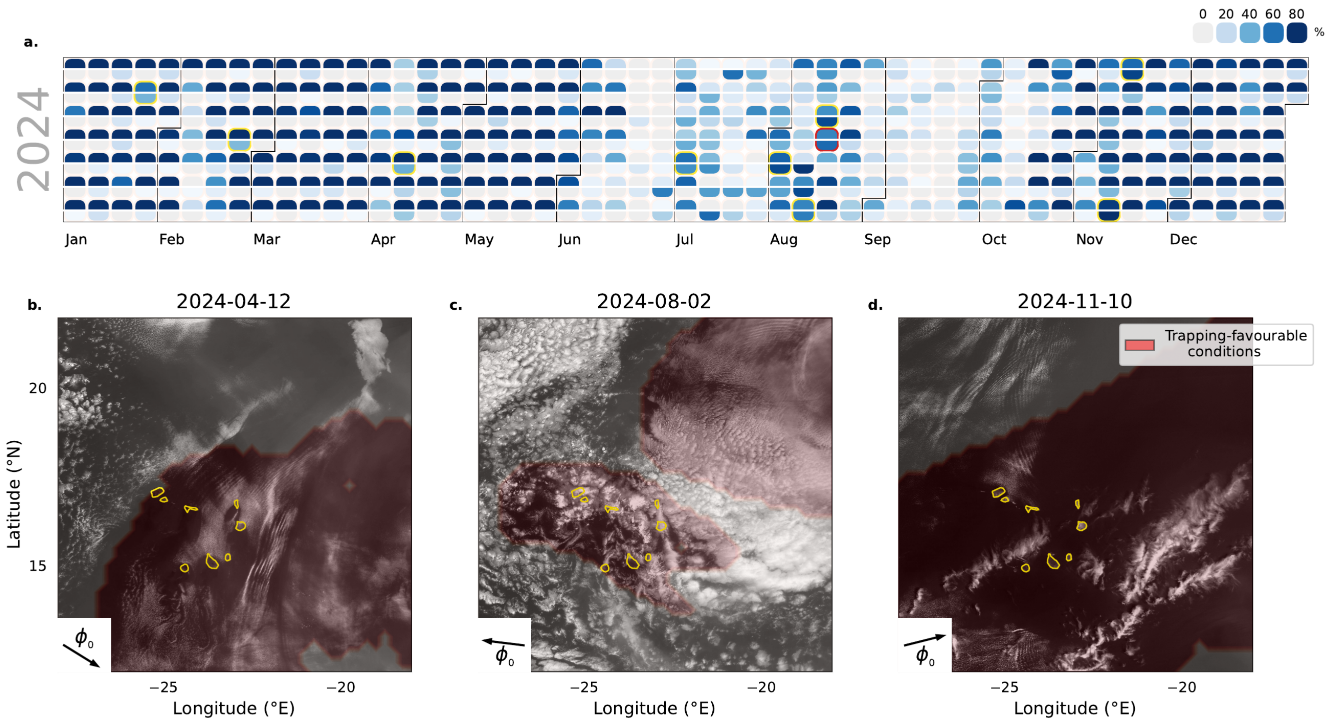

Figure 8. (a) Upper- and lower-TraLI, calculated over the 28° – 18° W, 12° – 22° N region in 2024. The day of our case study, 15 August 2024, is outlined in red, while other days featuring particularly large TraLI values are outlined in yellow. These selected days all exhibit clear wave activity in GOES-16 visible imagery, as illustrated by the snapshots for (b) 12 April, (c) 2 August and (d) 10 November 2024. In panels b-d, the semi-transparent red shading indicates the geographic location of the profiles belonging to the set $\mathscr{A}$ (Eq. 15), the direction of domain-averaged upper tropospheric flow ϕ_0 is shown in the lower-left corner and the coastline is represented as a solid yellow line.

ϕ_0. Figure 8c reveals wave activity within $\mathscr{A}$ (21° W, 21° N), but with distinct circular fronts that do not exhibit a preferred orientation consistent with ϕ_0, while Figure 8d shows a wave pattern whose orientation is well aligned with ϕ_0, but extending beyond the boundaries of $\mathscr{A}$ (26 – 23° W, 17 – 22° N). Overall, the frequent alignment of observed wave pattern orientations with the direction of ϕ_0 supports the validity of hypothesis (3). This highlights a key strength of the simplified Scorer parameter S_0: it serves a dual purpose, mapping the spatial (through $\mathscr{A}$) and temporal (via TraLI) likelihood of free-tropospheric wave trapping and simultaneously capturing the likely orientation of trapped waves.

Figure 8a displays strikingly different variability for the upper- and lower-TraLI. The upper-TraLI exhibits a significant seasonal cycle, with large values (over 80%) throughout most of the November-May period, indicating conditions favourable for the persistent and widespread occurrence of upper-tropospheric reflecting layers, interrupted only by occasional week-long breaks. Overall, this behaviour is driven by the pronounced seasonal cycle of the large-scale background winds, consistent with previous studies that linked the seasonality of GW trapping to that of large-scale winds (Stephan, 2020; Vicari et al., 2024). Indeed, during the November-May period, strong upper-tropospheric westerlies opposing the low-level easterlies (Fink et al.,

https://doi.org/10.5194/egusphere-2026-4254
Preprint. Discussion started: 3 September 2026

2017) are likely to favour upper-level wave reflection. Conversely, from June to October, the background wind shear weakens, leading to a general reduction in trapping likelihood; however, occasional maxima in upper-TraLI coincide well with periods of detected wave activity. This seasonal cycle is consistently found in all other analyzed years; notably, 2024 stands out because of its anomalously large upper-TraLI values in August.

In contrast, large values of the lower-TraLI appear highly intermittent, although more frequently observed in July and August. Due to this intermittency, the lower-TraLI plays a critical role in identifying free-tropospheric wave trapping events (days outlined in yellow in Figure 8a). The enhanced occurrence of large lower-TraLI values during July-August can be associated with the advection of the SAL over the Cape Verde region, with boreal summer representing the peak season for such long-range transport of Saharan dust (Gutleben et al., 2019). The weak stratification induced by mixing within the SAL can favour the formation of lower-tropospheric reflecting layers, consistent with the conditions observed in our 15 August 2024 case study.

5 Summary and discussion

As key takeouts from this study, we highlight the comprehensive characterization of a wave trapping event, and the importance of a large-scale, background wave duct to determine the wave characteristics, rather than the specificities of a source. We propose a Trapping Likelihood Index (TraLI), simplified from the Scorer parameter, in order to easily evaluate environments favourable to trapping. These findings are summarized in their respective subsections below, discussing first the case study and its implications, then the generalization.

5.1 Case-study and future observation possibilities

This study provides a uniquely detailed characterization of gravity waves trapped within an elevated layer in the free troposphere. The event is comprehensively described by combining in situ and remote-sensing airborne observations with radiosonde measurements and satellite imagery. A wave packet consisting of a half-dozen oscillations with 6.5 km horizontal wavelength and consistent signatures in vertical velocity (~ 1 m s^{-1} amplitude) and potential temperature (~ 1.2 K) is documented. A waveguide entirely decoupled from the surface is clearly identified in the vertical profile of the Scorer parameter (Nappo, 2012), extending between 5 and 10 km altitude. This is in contrast to the more commonly documented cases of waves trapped between the ground and a single tropospheric layer (Crook, 1988; Monserrat and Thorpe, 1996; Nappo, 2012). Overall, these observations point towards a trapped GW packet, and contrast with the strongly nonlinear sawtooth signature sampled for Kelvin-Helmholtz instability (see Appendix A).

The remarkable spatio-temporal coherence of the wave packets observed on 15 August suggests that these disturbances are not merely transient responses to localized sources. We evaluated several potential triggering mechanisms, including dry and moist convection, wind shear, and orography. While all these forcings were present to some extent on that day, none appears conspicuous or uniquely consistent with the observed wave field. For example, orographic waves remained generally confined

https://doi.org/10.5194/egusphere-2026-4254
Preprint. Discussion started: 3 September 2026

to the lee side of the Cape Verde islands, while the most significant deep convective event over the region was located to the southeast, thereby incompatible with the inferred direction of horizontal phase propagation.

Consequently, although a forcing mechanism is necessary to generate GWs, we argue that the primary factor determining the properties of the wave field is not the nature, the strength or the variability of the source, but the characteristics of the large-scale environment. The presence of a wave duct can sustain wave propagation and maintenance regardless of the initial source (Monserrat and Thorpe, 1996) or even in the absence of a continuous or energetic forcing (Lindzen and Tung, 1976; Román-Cascón et al., 2015). Thus, the identification of a specific triggering mechanism appears secondary to the characterization of the large-scale environmental conditions and the sampled signatures primarily reflect the selective filtering operated by the waveguide.

These observations constitute an essential complement to the recent study of Vicari et al. (2024), based primarily on remote-sensing and reanalysis data, in which the authors identified trapped wave signatures at regional scales, linking them to the background atmospheric state. Given the absence of in situ measurements, that study necessarily left some aspects unconstrained. The present observations help fill this gap by providing more direct constraints on the vertical structure of the waveguide and on key dynamical quantities that cannot be retrieved from remote sensing alone, e.g. the wave phase speed. This enables a thorough characterization of the wave-environment interactions sustaining the trapped modes. More broadly, the combination of satellite and in situ observations could provide a detailed characterization of the vertical velocity field, which, beyond the understanding of the atmospheric circulation, also has value for high-resolution global models, resolving a wider range of motions at the mesoscale that still require validation (Stephan et al., 2022).

5.2 Generalizing the analysis: a proxy for the Scorer parameter

Building on the physical understanding gained from the 15 August case study and on past studies of horizontal wave propagation, we propose a Trapping Likelihood Index (TraLI) to extend the analysis to a regional climatological perspective. This index relies on a simplification of the Scorer parameter, whose derivation purposefully defines a conservative criterion for the occurrence of trapping, retaining the upper-tropospheric shear-related reflection mechanism identified as dominant here and in previous studies (Stephan, 2020; Vicari et al., 2024). Within the chosen domain, TraLI quantifies the fraction of atmospheric profiles allowing for lower- and upper-level wave reflection, indicative of whether the large-scale environment can act as a free-tropospheric waveguide.

In our study region, TraLI successfully captures the occurrence of trapped GW events (including 15 August 2024) and shows a seasonal cycle overall consistent with those reported by previous investigations of GW trapping (Stephan, 2020; Vicari et al., 2024). As on 15 August, during boreal summer, large-scale trapping is often associated with a joint thermal-wind duct, whose lower boundary is defined by the weak stratification within an advected Saharan Air Layer, while the upper boundary is associated with vertical shear. Such a configuration appears specific to this region and season.

Keeping in mind that further evaluation of the robustness and broad applicability of TraLI is required, we note that our method can easily and readily provide a trapping likelihood assessment over any spatio-temporal domain. Likewise, the choice of reflection levels and critical wavelength can be adapted to target different trapping configurations (e.g. boundary layer ducts).

https://doi.org/10.5194/egusphere-2026-4254
Preprint. Discussion started: 3 September 2026

Finally, TraLI can in principle be computed from any observational or model-derived dataset, provided that spatial coverage and vertical resolution are sufficient. Regarding uncertainties in the chosen dataset (in our case, ERA5 reanalysis), TraLI is defined as a regional aggregate rather than a point-wise quantity, making it comparatively less sensitive to errors in individual atmospheric profiles.

By providing a simple yet meaningful way of systematically characterizing atmospheric conditions favourable to GW trapping over extended spatial and temporal scales, TraLI may facilitate investigations of whether trapped GW activity systematically co-varies with other atmospheric processes, such as changes in the radiative budget, moisture and cloud variability, and convective organization. This could help clarify the importance of trapping and contribute to addressing some long-standing challenges of studying tropospheric gravity waves globally: they are only one among many active processes, their signature is clearest in the vertical velocity field, particularly 'noisy' and difficult to observe, and they occur on short scales (down to the kilometer). Recent advancements in observing (Poujol and Bony, 2024) and simulating vertical motions (Stephan, 2020) open the way for investigating their potential importance for tropospheric dynamics and energetics.

Appendix A: In situ airborne observations of a Kelvin-Helmholtz instability case

In contrast to the clear linear wave signal documented on 15 August 2024, a strongly asymmetric signature associated with a Kelvin-Helmholtz instability (KHI) was sampled in situ on 25 August 2024. The along-track wind perturbations u', v' and w' (Figure A1a,b) indeed display highly non-linear oscillations consistent with a shear-driven instability (e.g. Stull, 1988). The nearest radiosounding, performed less than 30 km away at coinciding time, reveals a gradient Richardson number $\mathrm{Ri} < 0.25$ exactly at the flight altitude, spanning a layer of approximately 100 m depth (Figure A1c). The observed horizontal scale of the Kelvin-Helmholtz billows of around 500 m would correspond to an aspect ratio of 1 : 5, consistent with previous literature (Geerts and Miao, 2010). We also notice that the horizontal wind perturbations u' and v' exhibit a distinct low-frequency modulation, though its detailed analysis is beyond the scope of the present appendix.

Overall, given the scarcity of in situ observations of KHI in the real atmosphere – with Nielsen (1992) representing to our knowledge one of the very few documented exceptions – the event sampled on 25 August 2024 will offer a uniquely detailed framework to investigate the fine structure of Kelvin-Helmholtz billows thanks to the comprehensive suite of instruments onboard the ATR-42.

Data availability. The data from the MAESTRO field campaign are freely available at https://maestro.aeris-data.fr. For the ORCESTRA radiosonde observations the reader is referred to the data availability statement of Winkler et al. (2026). GOES-16 satellite products and ERA5 reanalysis data are publicly available at https://noaa-goes16.s3.amazonaws.com/index.html and https://cds.climate.copernicus.eu, respectively.

https://doi.org/10.5194/egusphere-2026-4254
Preprint. Discussion started: 3 September 2026

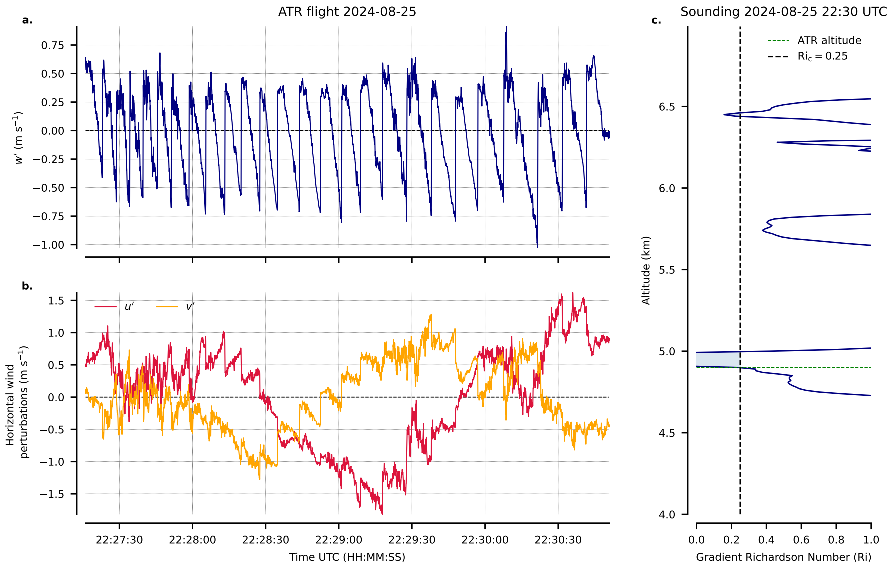

Figure A1. In situ airborne sampling of a Kelvin-Helmholtz instability case on 25 August 2024, during a straight, level leg at 4.9 km altitude. (a,b) Perturbations of vertical (w', blue), zonal (u', red) and meridional (v', orange) velocities relative to the along-track background. (c) Vertical profile of the gradient Richardson number (Ri) obtained from the closest radiosounding (see text for details). To compute Ri, a local least-square third-order polynomial filter with a 500 m window was applied to the vertical profiles of θ_v, u and v. The dashed vertical line denotes the critical value $\mathrm{Ri}_c = 0.25$ for shear-driven instability. The flight altitude is shown as a dashed green horizontal line.

Author contributions. The first two authors designed the study, performed the analysis, and wrote the original draft. RP supervised the research. SB acquired the funding and led the operations of the MAESTRO field campaign. RP and SB reviewed and edited the manuscript.

Competing interests. The authors declare that they have no conflict of interest.

Acknowledgements. This project has received funding from the European Research Council (ERC) under the European Union's Horizon 2020 research and innovation programme (MAESTRO Advanced Grant agreement No 101098063), from the CNES EMC-Sat grant, and from École polytechnique.

https://doi.org/10.5194/egusphere-2026-4254
Preprint. Discussion started: 3 September 2026

References

Achatz, U., Alexander, M. J., Becker, E., Chun, H.-Y., Dörnbrack, A., Holt, L., Plougonven, R., Polichtchouk, I., Sato, K., Sheshadri, A., Stephan, C. C., van Niekerk, A., and Wright, C. J.: Atmospheric Gravity Waves: Processes and Parameterization, Journal of the Atmospheric Sciences, 81, 237 – 262, https://doi.org/10.1175/JAS-D-23-0210.1, 2024.

Alexander, M., Geller, M., McLandress, C., Polavarapu, S., Preusse, P., Sassi, F., Sato, K., Eckermann, S., Ern, M., Hertzog, A., et al.: Recent developments in gravity-wave effects in climate models and the global distribution of gravity-wave momentum flux from observations and models, Quarterly Journal of the Royal Meteorological Society, 136, 1103–1124, 2010.

Alexander, P., de la Torre, A., Llamedo, P., Hierro, R., Marcos, T., Kaifler, B., Kaifler, N., Geldenhuys, M., Preusse, P., Giez, A., Rapp, M., and Hormaechea, J. L.: The Coexistence of Gravity Waves From Diverse Sources During a SOUTHTRAC Flight, Journal of Geophysical Research: Atmospheres, 128, e2022JD037 276, https://doi.org/https://doi.org/10.1029/2022JD037276, e2022JD037276, 2023.

Andrews, D. G., Holton, J. R., and Leovy, C. B.: Middle Atmosphere Dynamics, Academic Press, ISBN 9780120585762, 1987.

Atlas, R., Podglajen, A., Wilson, R., Hertzog, A., and Plougonven, R.: Turbulence in the tropical stratosphere, equatorial Kelvin waves, and the Quasi-Biennial Oscillation, Proceedings of the National Academy of Sciences, 122, e2409791 122, 2025.

Balaji, V. and Clark, T. L.: Scale selection in locally forced convective fields and the initiation of deep cumulus, J. Atmos. Sci., 45, 3189–3211, 1988.

Bölöni, G., Kim, Y.-H., Borchert, S., and Achatz, U.: Toward transient subgrid-scale gravity wave representation in atmospheric models. Part I: Propagation model including nondissipative wave–mean-flow interactions, Journal of the Atmospheric Sciences, 78, 1317–1338, 2021.

Bony, S., Lothon, M., Delanoë, J., Coutris, P., Etienne, J.-C., Aemisegger, F., Albright, A. L., André, T., Bellec, H., Baron, A., Bourdinot, J.-F., Brilouet, P.-E., Bourdon, A., Canonici, J.-C., Caudoux, C., Chazette, P., Cluzeau, M., Cornet, C., Desbios, J.-P., Duchanoy, D., Flamant, C., Fildier, B., Gourbeyre, C., Guiraud, L., Jiang, T., Lainard, C., Le Gac, C., Lendroit, C., Lernould, J., Perrin, T., Pouvesle, F., Richard, P., Rochetin, N., Salaün, K., Schwarzenboeck, A., Seurat, G., Stevens, B., Totems, J., Touzé-Peiffer, L., Vergez, G., Vial, J., Villiger, L., and Vogel, R.: EUREC^{4}A observations from the SAFIRE ATR42 aircraft, Earth System Science Data, 14, 2021–2064, https://doi.org/10.5194/essd-14-2021-2022, 2022.

Carlson, T. N. and Prospero, J. M.: The Large-Scale Movement of Saharan Air Outbreaks over the Northern Equatorial Atlantic, Journal of Applied Meteorology and Climatology, 11, 283 – 297, https://doi.org/10.1175/1520-0450(1972)011<0283:TLSMOS>2.0.CO;2, 1972.

Crook, N. A.: Trapping of Low-Level Internal Gravity Waves, Journal of Atmospheric Sciences, 45, 1533 – 1541, https://doi.org/10.1175/1520-0469(1988)045<1533:TOLLIG>2.0.CO;2, 1988.

Dong, W., Hickey, M. P., and Zhang, S.: A Numerical Study of Gravity Waves Propagation Characteristics in the Mesospheric Doppler Duct, Journal of Geophysical Research: Atmospheres, 126, e2021JD034 680, https://doi.org/https://doi.org/10.1029/2021JD034680, e2021JD034680 2021JD034680, 2021.

Dörnbrack, A., Birner, T., Fix, A., Flentje, H., Meister, A., Schmid, H., Browell, E. V., and Mahoney, M. J.: Evidence for inertia gravity waves forming polar stratospheric clouds over Scandinavia, Journal of Geophysical Research: Atmospheres, 107, SOL–30, 2002.

Durran, D. R.: Do breaking mountain waves deceierate the local mean flow?, Journal of Atmospheric Sciences, 52, 4010–4032, 1995.

Ern, M., Preusse, P., Alexander, M. J., and Warner, C. D.: Absolute values of gravity wave momentum flux derived from satellite data, Journal of Geophysical Research: Atmospheres, 109, 2004.

Fink, A. H., Engel, T., Ermert, V., van der Linden, R., Schneidewind, M., Redl, R., Afiesimama, E., Thiaw, W. M., Yorke, C., Evans, M., and Janicot, S.: Mean Climate and Seasonal Cycle, chap. 1, pp. 1–39, John Wiley & Sons, Ltd, ISBN 9781118391297, https://doi.org/https://doi.org/10.1002/9781118391297.ch1, 2017.

Fritts, D. C. and Alexander, M. J.: Gravity wave dynamics and effects in the middle atmosphere, Reviews of Geophysics, 41, https://doi.org/https://doi.org/10.1029/2001RG000106, 2003.

Fritts, D. C., Nappo, C., Riggin, D. M., Balsley, B. B., Eichinger, W. E., and Newsom, R. K.: Analysis of ducted motions in the stable nocturnal boundary layer during CASES-99, Journal of the Atmospheric Sciences, 60, 2450–2472, 2003.

Geerts, B. and Miao, Q.: Vertically Pointing Airborne Doppler Radar Observations of Kelvin–Helmholtz Billows, Monthly Weather Review, 138, 982 – 986, https://doi.org/10.1175/2009MWR3212.1, 2010.

Georgelin, M. and Lott, F.: On the transfer of momentum by trapped lee waves: Case of the IOP 3 of PYREX, Journal of the atmospheric sciences, 58, 3563–3580, 2001.

Glanville, A. A. and Birner, T.: Role of vertical and horizontal mixing in the tape recorder signal near the tropical tropopause, Atmospheric Chemistry and Physics, 17, 4337–4353, 2017.

Gretarsson, A. M.: Optical Cavities, in: A First Course in Laboratory Optics, vol. 102, pp. 133–151, Cambridge University Press, 2021.

Guest, F. M., Reeder, M. J., Marks, C. J., and Karoly, D. J.: Inertia–Gravity Waves Observed in the Lower Stratosphere over Macquarie Island, Journal of the Atmospheric Sciences, 57, 737 – 752, https://doi.org/10.1175/1520-0469(2000)057<0737:IGWOIT>2.0.CO;2, 2000.

Gutleben, M., Groß, S., Wirth, M., Emde, C., and Mayer, B.: Impacts of Water Vapor on Saharan Air Layer Radiative Heating, Geophysical Research Letters, 46, 14 854–14 862, https://doi.org/https://doi.org/10.1029/2019GL085344, 2019.

Hersbach, H., Bell, B., Berrisford, P., Hirahara, S., Horányi, A., Muñoz-Sabater, J., Nicolas, J., Peubey, C., Radu, R., Schepers, D., Simmons, A., Soci, C., Abdalla, S., Abellan, X., Balsamo, G., Bechtold, P., Biavati, G., Bidlot, J., Bonavita, M., Chiara, G., Dahlgren, P., Dee, D., Diamantakis, M., Dragani, R., Flemming, J., Forbes, R., Fuentes, M., Geer, A., Haimberger, L., Healy, S., Hogan, R. J., Hólm, E., Janisková, M., Keeley, S., Laloyaux, P., Lopez, P., Lupu, C., Radnoti, G., Rosnay, P., Rozum, I., Vamborg, F., Villaume, S., and Thépaut, J.-N.: The ERA5 global reanalysis, Quarterly Journal of the Royal Meteorological Society, 146, 1999–2049, https://doi.org/10.1002/qj.3803, 2020.

Hoffmann, L., Xue, X., and Alexander, M.: A global view of stratospheric gravity wave hotspots located with Atmospheric Infrared Sounder observations, Journal of Geophysical Research: Atmospheres, 118, 416–434, 2013.

Isler, J. R., Taylor, M. J., and Fritts, D. C.: Observational evidence of wave ducting and evanescence in the mesosphere, Journal of Geophysical Research: Atmospheres, 102, 26 301–26 313, https://doi.org/10.1029/97JD01783, 1997.

Jaffeux, L., Lothon, M., Couvreux, F., Bouniol, D., Cayez, G., Joly, L., Burgalat, J., De Saint Leger, C., Bellec, H., Henry, O., Chbib, D., Jiang, T., and Bony, S.: The MAESTRO turbulence dataset derived from the SAFIRE ATR42 aircraft, Earth System Science Data Discussions, 2025, 1–31, https://doi.org/10.5194/essd-2025-586, 2025.

Jensen, E. J., Ueyama, R., Pfister, L., Bui, T. V., Alexander, M. J., Podglajen, A., Hertzog, A., Woods, S., Lawson, R. P., Kim, J.-E., et al.: High-frequency gravity waves and homogeneous ice nucleation in tropical tropopause layer cirrus, Geophysical Research Letters, 43, 6629–6635, 2016.

Jia, M., Yuan, J., Wang, C., Xia, H., Wu, Y., Zhao, L., Wei, T., Wu, J., Wang, L., Gu, S.-Y., Liu, L., Lu, D., Chen, R., Xue, X., and Dou, X.: Long-lived high-frequency gravity waves in the atmospheric boundary layer: observations and simulations, Atmospheric Chemistry and Physics, 19, 15 431–15 446, https://doi.org/10.5194/acp-19-15431-2019, 2019.

https://doi.org/10.5194/egusphere-2026-4254
Preprint. Discussion started: 3 September 2026

Kim, J.-H., Chan, W. N., Sridhar, B., and Sharman, R. D.: Combined Winds and Turbulence Prediction System for Automated Air-Traffic Management Applications, Journal of Applied Meteorology and Climatology, 54, 766 – 784, https://doi.org/10.1175/JAMC-D-14-0216.1, 2015.

Knop, I., Dolaptchiev, S., and Achatz, U.: Impact of small-scale gravity waves on tracer transport, Quarterly Journal of the Royal Meteorological Society, 152, e70 091, https://doi.org/10.1002/qj.70091, 2026.

Konopka, P., Günther, G., Müller, R., Dos Santos, F., Schiller, C., Ravegnani, F., Ulanovsky, A., Schlager, H., Volk, C., Viciani, S., et al.: Contribution of mixing to upward transport across the tropical tropopause layer (TTL), Atmospheric Chemistry and Physics, 7, 3285–3308, 2007.

Kottayil, A., Podglajen, A., Legras, B., Atlas, R., K, P., Satheesan, K., and S, A.: High-Frequency Gravity Waves and Kelvin-Helmholtz Billows in the Tropical UTLS, as Seen From Radar Observations of Vertical Wind, Geophysical Research Letters, 51, e2024GL110 366, https://doi.org/https://doi.org/10.1029/2024GL110366, e2024GL110366 2024GL110366, 2024.

Lane., T. P. and Clark, T. L.: Gravity waves generated by the dry convective boundary layer: Two-dimensional scale selection and boundary-layer feedback, Quarterly Journal of the Royal Meteorological Society, 128, 1543–1570, https://doi.org/https://doi.org/10.1002/qj.200212858308, 2002.

Lane, T. P. and Zhang, F.: Coupling between Gravity Waves and Tropical Convection at Mesoscales, Journal of the Atmospheric Sciences, 68, 2582 – 2598, https://doi.org/10.1175/2011JAS3577.1, 2011.

Lindzen, R. S. and Tung, K.-K.: Banded Convective Activity and Ducted Gravity Waves, Monthly Weather Review, 104, 1602 – 1617, https://doi.org/10.1175/1520-0493(1976)104<1602:BCAADG>2.0.CO;2, 1976.

Lu, C., Koch, S., and Wang, N.: Determination of temporal and spatial characteristics of atmospheric gravity waves combining cross-spectral analysis and wavelet transformation, Journal of Geophysical Research: Atmospheres, 110, https://doi.org/https://doi.org/10.1029/2004JD004906, 2005.

Luce, H., Kantha, L., Yabuki, M., and Hashiguchi, H.: Atmospheric Kelvin–Helmholtz billows captured by the MU radar, lidars and a fish-eye camera, Earth, Planets and Space, 70, https://doi.org/10.1186/s40623-018-0935-0, 2018.

Ludlam, F. H.: Characteristics of billow clouds and their relation to clear-air turbulence, Quarterly Journal of the Royal Meteorological Society, 93, 419–435, https://doi.org/https://doi.org/10.1002/qj.49709339803, 1967.

Matsuno, T.: Quasi-Geostrophic Motions in the Equatorial Area, Journal of the Meteorological Society of Japan. Ser. II, 44, 25–43, https://doi.org/10.2151/jmsj1965.44.1_25, 1966.

Monserrat, S. and Thorpe, A. J.: Use of Ducting Theory in an Observed Case of Gravity Waves, Journal of Atmospheric Sciences, 53, 1724 – 1736, https://doi.org/10.1175/1520-0469(1996)053<1724:UODTIA>2.0.CO;2, 1996.

Nappo, C. J.: An Introduction to Atmospheric Gravity Waves, vol. 102, Academic press, 2012.

Nielsen, J. W.: In Situ Observations of Kelvin-Helmholtz Waves along a Frontal Inversion, Journal of Atmospheric Sciences, 49, 369 – 386, https://doi.org/10.1175/1520-0469(1992)049<0369:ISOOKH>2.0.CO;2, 1992.

Nishi, A. and Sugawara, H.: Effect of trapped lee wave interference on the shape of wave clouds, Quarterly Journal of the Royal Meteorological Society, 152, e70 226, https://doi.org/https://doi.org/10.1002/qj.70226, 2026.

Plougonven, R., Teitelbaum, H., and Zeitlin, V.: Inertia gravity wave generation by the tropospheric midlatitude jet as given by the Fronts and Atlantic Storm-Track Experiment radio soundings, Journal of Geophysical Research: Atmospheres, 108, https://doi.org/https://doi.org/10.1029/2003JD003535, 2003.

https://doi.org/10.5194/egusphere-2026-4254
Preprint. Discussion started: 3 September 2026

Plougonven, R., Hertzog, A., and Teitelbaum, H.: Observations and simulations of a large-amplitude mountain wave breaking over the Antarctic Peninsula, Journal of Geophysical Research: Atmospheres, 113, https://doi.org/https://doi.org/10.1029/2007JD009739, 2008.

Poujol, B. and Bony, S.: Measuring Clear-Air Vertical Motions From Space, AGU Advances, 5, e2024AV001 267, https://doi.org/https://doi.org/10.1029/2024AV001267, e2024AV001267 2024AV001267, 2024.

Queney, P.: The problem of air flow over mountains: A summary of theoretical studies, Bulletin of the American Meteorological Society, 29, 16–26, 1948.

Román-Cascón, C., Yagüe, C., Viana, S., Sastre, M., Maqueda, G., Lothon, M., and Gómara, I.: "Near-monochromatic ducted gravity waves associated with a convective system close to the Pyrenees", Quarterly Journal of the Royal Meteorological Society, 141, 1320–1332, https://doi.org/https://doi.org/10.1002/qj.2441, 2015.

Schmit, T. J., Griffith, P., Gunshor, M. M., Daniels, J. M., Goodman, S. J., and Lebair, W. J.: A Closer Look at the ABI on the GOES-R Series, Bulletin of the American Meteorological Society, 98, 681 – 698, https://doi.org/10.1175/BAMS-D-15-00230.1, 2017.

Scorer, R. S.: Theory of waves in the lee of mountains, Quarterly Journal of the Royal Meteorological Society, 75, 41–56, https://doi.org/https://doi.org/10.1002/qj.49707532308, 1949.

Stephan, C. C.: Seasonal Modulation of Trapped Gravity Waves and Their Imprints on Trade Wind Clouds, Journal of the Atmospheric Sciences, 77, 2993 – 3009, https://doi.org/10.1175/JAS-D-19-0325.1, 2020.

Stephan, C. C., Duras, J., Harris, L., Klocke, D., Putman, W. M., Taylor, M., Wedi, N., Žagar, N., and Ziemen, F.: Atmospheric energy spectra in global kilometre-scale models, Tellus A: Dynamic Meteorology and Oceanography, 74, 2022.

Stevens, B., Bony, S., Gross, S., Klocke, D., Windmiller, J. M., Wing, A. A., von Bismarck, J., Brito, E., David, R. O., Delanoë, J., Farrell, D., and Wu, Y.: ORCESTRA: Organized Convection and EarthCARE Studies Over the Tropical Atlantic, Tellus, 79, 35–52, https://doi.org/10.16993/tellus.4123, 2026.

Stull, R. B., ed.: An Introduction to Boundary Layer Meteorology, Springer Dordrecht, https://doi.org/https://doi.org/10.1007/978-94-009-3027-8, 1988.

Teixeira, M. A. and Argaín, J. L.: The drag exerted by weakly dissipative trapped lee waves on the atmosphere: Application to Scorer's two-layer model, Quarterly Journal of the Royal Meteorological Society, 148, 3211–3230, 2022.

Thorpe, S. A.: Experiments on the Stability of Stratified Shear Flows, Radio Science, 4, 1327–1331, https://doi.org/https://doi.org/10.1029/RS004i012p01327, 1969.

Thorpe, S. A.: Experiments on the instability of stratified shear flows: miscible fluids, Journal of Fluid Mechanics, 46, 299–319, https://doi.org/10.1017/S0022112071000557, 1971.

Trier, S. B. and Sharman, R. D.: Trapped gravity waves and their association with turbulence in a large thunderstorm anvil during PECAN, Monthly Weather Review, 146, 3031–3052, 2018.

Vicari, R., Stephan, C. C., Lane, T. P., and Huang, Y.: Analysis of Trapped Small-Scale Internal Gravity Waves Automatically Detected in Satellite Imagery, Journal of Geophysical Research: Atmospheres, 129, e2023JD038 956, https://doi.org/https://doi.org/10.1029/2023JD038956, e2023JD038956 2023JD038956, 2024.

Wheeler, M. and Kiladis, G. N.: Convectively Coupled Equatorial Waves: Analysis of Clouds and Temperature in the Wavenumber–Frequency Domain, Journal of the Atmospheric Sciences, 56, 374 – 399, https://doi.org/10.1175/1520-0469(1999)056<0374:CCEWAO>2.0.CO;2, 1999.

Winkler, M., Rixen, M., Beucher, F., Couvreux, F., Nam, C. C., Peyrillé, P., Schmidt, H., Segura, H., Wieners, K.-H., Alkilani-Brown, E., Coly, A. A., Biagioli, G., Bell, M. M., Brito, E., Chauvin, E., Capo, J., Colón-Burgos, D., Dawes, A., da Luz, J. C., Demiralay, Z., Douet,

https://doi.org/10.5194/egusphere-2026-4254
Preprint. Discussion started: 3 September 2026

V., Ducastin, V., Dufaux, C., Dufresne, J.-L., Favot, F., Fiolleau, T., Fons, E., George, G., Gloeckner, H. M., Gonçalves, S., Gouttesoulard, L., Hayo, L., Hsiao, W.-T., Kennison, S., Kopelman, M., Lee, T.-Y., Le Gall, E., Lovato, M., Luschen, E., Maury, N., McKim, B., Netz, L., Ousseynou, D., Peters-von Gehlen, K., Pope, C., Poujol, B., Rivera Maldonado, N., Robbins-Blanch, N., Rochetin, N., Rowe, D., Romero Jure, P., Ruppert Jr., J. H., Segura Bermudez, J., Starr, J. C., Stelzner, M., Stoll, C., Syrett, M., Tekoe, A., Trules, J., Welty, C., Klocke, D., Vogel, R., Bony, S., Wing, A. A., and Stevens, B.: RAPSODI: radiosonde atmospheric profiles from ship and island platforms during ORCESTRA, collected to Decipher the ITCZ, Earth System Science Data, 18, 1833–1854, https://doi.org/10.5194/essd-18-1833-2026, 2026.

Wurtele, M., Sharman, R., and Datta, A.: Atmospheric lee waves, Annual review of fluid mechanics, pp. 429–476, 1996.